Abundance and Sources of Atmospheric Halocarbons in the Eastern Mediterranean

Fabian Schoenenberger[1], Stephan Henne[1], Matthias Hill[1], Martin K. Vollmer[1],
Giorgos Kouvarakis[2], Nikolaos Mihalopoulos[2], Simon O'Doherty[3], Michela Maione[4],
5   Lukas Emmenegger[1], Thomas Peter[5], Stefan Reimann[1]

[1]Laboratory for Air Pollution/Environmental Technologies, Empa, Swiss Federal Laboratories for Materials
Science and Technology, Dübendorf, Switzerland
[2]Department of Chemistry, University of Crete, Heraklion Crete, Greece
10   [3]School of Chemistry, University of Bristol, Bristol, UK
[4]Department of Pure and Applied Sciences, University of Urbino, Urbino, Italy
[5]Institute for Atmospheric and Climate Science, ETH Zürich, Zürich, Switzerland

Correspondence to: Fabian Schoenenberger (fabian.schonenberger@gmail.com)

15   Abstract

A wide range of anthropogenic halocarbons is released to the atmosphere, contributing to stratospheric ozone depletion and global warming. Using measurements of atmospheric abundances for the estimation of halocarbon emissions on the global and regional scale has become an important top-down tool for emission validation in the recent past, but many populated and developing areas of the world are only poorly covered by the existing atmospheric halocarbon measurement network. Here we present six months of continuous halocarbon observations from Finokalia on the island of Crete in the Eastern Mediterranean. The gases measured are the hydrofluorocarbons (HFCs), HFC-134a (CH_2FCF_3), HFC-125 (CHF_2CF_3), HFC-152a (CH_3CHF_2) and HFC-143a (CH_3CF_3), and the hydrochlorofluorocarbons (HCFCs), HCFC-22 ($CHClF_2$) and HCFC-142b (CH_3CClF_2). The Eastern Mediterranean is home to 250 million inhabitants, consisting of a number of developed and developing countries, for which different emission regulations exist under the Kyoto and Montreal Protocols. Regional emissions of halocarbons were estimated with Lagrangian atmospheric transport simulations and a Bayesian inverse modelling system, using measurements at Finokalia in conjunction with those from Advanced Global Atmospheric Gases Experiment (AGAGE) sites at Mace Head (Ireland), Jungfraujoch (Switzerland) and Monte Cimone (Italy). Measured peak mole fractions at Finokalia showed generally smaller amplitudes for HFCs than at the European AGAGE sites, except periodic peaks of HFC-152a, indicating strong upwind sources. Higher peak mole fractions were observed for HCFCs, suggesting continued emissions from nearby developing regions such as Egypt and the Middle East. For 2013, the Eastern Mediterranean inverse emission estimates for the four analysed HFCs and the two HCFCs were 14.7 (6.7-23.3) Tg CO_2eq yr^{-1} and 9.7 (4.3-15.7) Tg CO_2eq yr^{-1}, respectively. These emissions contributed 17.3% (7.9-27.4%) and 53% (23.5-86%) to the total inversion domain, which covers the Eastern Mediterranean as well as Central and Western Europe. Greek bottom-up HFC emissions reported to the UNFCCC were much smaller than our top-down estimates, whereas for Turkey our estimates agreed with UNFCCC-reported values for HFC-125 and HFC-143a, but were much and slightly smaller for HFC-134a and HFC-152a, respectively. Sensitivity estimates suggest an improvement of the a posteriori emission estimates, i.e. a reduction of the uncertainties by 40-80%, compared to an inversion using only the existing Central European AGAGE observations.

1 Introduction

Anthropogenic halocarbons, i.e. chlorofluorocarbons (CFCs), hydrochlorofluorocarbons (HCFCs), hydrofluorocarbons (HFCs), halons and other brominated species, are used in a wide range of industrial and domestic applications (e.g., refrigeration, air conditioning, foam blowing, solvent usage, aerosol propellants and fire retardants). Whereas only chlorinated and brominated halocarbons are responsible for stratospheric ozone depletion, all long-lived halocarbons are potent greenhouse gases [*Molina and Rowland*, 1974; *Farman, et al.*, 1985; *Myhre, et al.*, 2013; *Carpenter and Reimann*, 2014].

50

Ozone depleting substances (ODSs) are regulated by the Montreal Protocol (MP), which resulted in the global phase-out of CFCs from emissive use by 2010. HCFCs, which serve as transitional replacement products, are subject to a less demanding multistep phase-out ending in 2030 for Non-Article-5 (developed) and 2040 for Article-5 (developing) countries [*Braathen, et al.*, 2012]. To track the development of CFC and HCFC emissions to the atmosphere, the MP requires signatory parties to produce an inventory of their ODS consumption and production [*McCulloch, et al.*, 2001].

55

HFCs, used as second-generation replacement products for ODSs, do not contain chlorine or bromine. However, as some of them have a large global warming potential (GWP) and a projected rapid increase in their emissions, HFCs may significantly contribute to global radiative forcing as a direct consequence of protecting the ozone layer [*Steinbacher, et al.*, 2008; *Velders, et al.*, 2012; *Rigby, et al.*, 2014; *Montzka, et al.*, 2015]. HFCs are addressed within the Kyoto Protocol to the United Nations Framework Convention on Climate Change (UNFCCC). Signatory parties with binding emission reduction targets (Annex I) are required to submit their HFC emission inventories to the UNFCCC [*UNFCCC*, 1997]. These inventories are based on statistical "bottom-up" estimates, using production and consumption data and have been suspected to carry significant uncertainties [e.g., *Levin, et al.*, 2010; *Keller, et al.*, 2012; *Rigby, et al.*, 2014; *Lunt, et al.*, 2015]. In 2016, HFCs were included in the Montreal Protocol by the Kigali Amendment, targeting a phase-down of the consumption to 15% of the original value.

60

65

70

To validate reported inventories, "top-down" approaches, based on atmospheric measurements and atmospheric transport and chemistry models can be used. The combination of observations with simplified global scale box-models, allows the independent derivation of global emissions [e.g., *Rigby, et al.*, 2010; *Carpenter and Reimann*, 2014; *Schoenenberger, et al.*, 2015; *Vollmer, et al.*, 2015]. The application of more detailed atmospheric models has proven to be a powerful

75

tool to quantify emissions on a spatially and temporally more explicit level enabling for emission estimates on a continental to country scale [e.g., *Manning, et al.*, 2003; *Stohl, et al.*, 2009; *Kim, et al.*, 2010; *Brunner, et al.*, 2012a; *Keller, et al.*, 2012; *Saikawa, et al.*, 2012; *Ganesan, et al.*, 2014; *Maione, et al.*, 2014; *Graziosi, et al.*, 2015; *Hu, et al.*, 2015; *Lunt, et al.*, 2015].

In Europe, the AGAGE network provides high-frequency observations of atmospheric halocarbons at 3 sites: Mace Head (Ireland), Zeppelin mountain (Spitsbergen, Norway), Jungfraujoch (Switzerland) and the affiliated station at Monte Cimone (Italy) [*Prinn, et al.*, 2000]. While data from this network have been frequently used in top-down estimates of Western European halocarbon emissions [e.g., *Reimann, et al.*, 2008; *Brunner, et al.*, 2012b; *Keller, et al.*, 2012], the network has a very limited sensitivity towards emission from Eastern European sources (Figure 1a). For Eastern European HFC emissions, the importance of extending the observational network was illustrated by the large discrepancies between bottom-up emissions reported to UNFCCC and those estimated top-down in an inverse modelling study using atmospheric observations obtained during a field campaign at K-Puszta in Hungary [*Keller, et al.*, 2012].

Even less reliable information on halocarbon emissions is available from the Eastern Mediterranean region, comprising Turkey, which is regarded as a developing country in the terminology of the Montreal Protocol (Article 5) but is a signatory party with binding emission reduction targets under the Kyoto Protocol (Annex I), Non-Article 5/Annex I states such as Greece, Romania, Bulgaria and Cyprus, and developing economies (Article 5/Non Annex I) such as Egypt and Israel with less stringent regulations and reporting requirements.

Estimating halocarbon emissions by top-down methods in the Eastern Mediterranean gains additional importance in the light of the beginning phase-out of HCFC emissions in Article-5 countries under the Montreal Protocol. This motivated our halocarbon measurement campaign at Finokalia (Crete, Greece) from December 2012 to August 2013. Here, we present the observed atmospheric halocarbon levels and combine the dataset with halocarbon observations at Jungfraujoch, Mace Head and Monte Cimone, atmospheric transport modelling and a Bayesian inversion system to derive the first comprehensive top-down emission estimates of HFC-134a (CH_2FCF_3), HFC-125 (CHF_2CF_3), HFC-152a (CH_3CHF_2), HFC-143a (CH_3CF_3), HCFC-22 ($CHClF_2$) and HCFC-142b (CH_3CClF_2) in the Eastern Mediterranean.

2 Methods

2.1 Observational Sites

Halocarbon measurements were conducted from December 2012 to August 2013 at the atmospheric observation site in Finokalia (FKL, 35.34°N, 25.67°E, 250 m a.s.l. [*Mihalopoulos, et al.,* 1997]), which is part of the "Aerosol, Clouds and Trace gases Research Infrastructure" (ACTRIS). The station is located on the northeastern coast of Crete on top of a hill, facing the Mediterranean Sea within a sector from 270° to 90°. It is surrounded by sparse vegetation and olive tree plantations, without significant human activity in the near vicinity, except a small village 3 km to the South. Heraklion, the closest, more densely populated area (~200'000 inhabitants), is situated approximately 50 km west of Finokalia.

Operational meteorological observations, such as wind speed, wind direction, temperature, relative humidity and solar radiation are available at the station. In addition to classical air quality parameters (ozone, nitrogen oxides, carbon monoxide) the station is equipped with a large suite of aerosol measurements.

The halocarbon observations at Finokalia were complemented with data from the AGAGE sites at Jungfraujoch and Mace Head and from Monte Cimone for this study. The high-altitude site Jungfraujoch (JFJ, 7.99°E, 46.55°N, 3573 m a.s.l.) is located in the northern Swiss Alps. It is usually exposed to free tropospheric air but can also be affected by polluted boundary layer air from both sides of the Alps [*Zellweger, et al.*, 2003; *Henne, et al.*, 2010; *Herrmann, et al.*, 2015]. The Mace Head observatory (MHD, 9.90°W, 53.33°N, 15 m a.s.l.) on the west coast of Ireland is normally exposed to relatively clean air from the North Atlantic Ocean but can also be influenced by continental European air masses under certain atmospheric transport conditions. Similar to Jungfraujoch the high-altitude site Monte Cimone (CMN, 10.70°E, 44.18°N, 2165 m a.s.l.) in the Apennine Mountains in Northern Italy is often situated in the lower free troposphere, but especially during daytime receives polluted boundary layer air [*Bonasoni, et al.*, 2000].

2.2 Analytical Methods

In situ measurements of halocarbons at the Finokalia observation site were conducted using a gas chromatograph (Agilent 6890) mass spectrometer (Agilent 5973) (GCMS), coupled to an adsorption desorption system (ADS) for pre-concentration of samples from the air [*Simmonds, et al.*, 1995]. A similar instrument is used at Monte Cimone [*Maione, et al.*, 2013]. The ADS is

the predecessor of the Medusa pre-concentration unit, which is currently used at the AGAGE sites Jungfraujoch and Mace Head [*Miller, et al.*, 2008].

Two litres of air were sampled every 2 hours, with a collection duration of 40 min, 2 m above
140   the rooftop of the station building, using an inlet facing the open sea. For the correction of short-term drifts of the mass spectrometer response, a working standard was measured after each 10th air sample analysis. Two such standards were used throughout the project, both real-air samples compressed into internally electro-polished 34 L stainless steel canisters (Essex Cryogenics, Missouri, USA) at Rigi-Seebodenalp (Switzerland), using an oil-free diving compressor. These
145   working standards were calibrated against standards provided by the Scripps Institution of Oceanography (SIO). All results are reported on SIO calibration scales and expressed as dry air mole fractions in parts per trillion (ppt), 10^{-12}. The respective scales are SIO-05 for HFC-134a, HFC-152a, HCFC-22 and HCFC-142b, SIO-07 for HFC-143a and SIO-14 for HFC-125.

The measurement precision, which is calculated separately for each compound, was estimated
150   as the standard deviation of the working standard observations, inside a moving window covering 10 standard measurements (SI-Table 1). Note that the precision for the ADS measurements at Finokalia was up to an order of magnitude worse than for the sites equipped with the Medusa system. This was partly caused by less frequent reference gas measurements by the ADS compared to the Medusa. Nevertheless, for the atmospheric inversion this reduction in
155   measurement precision can be tolerated, since the largest part of the total uncertainty in the inversion is contributed by uncertainties in the transport model.

2.3 Data Treatment

Data quality was ensured by examining chromatographic quality and comparing observed mole fractions to observations at selected European AGAGE sites (JFJ, MHD, CMN). Specific ob-
160   servations, showing poor chromatographic quality or unrealistic measurement behaviour were excluded from the time series.

Due to hardware problems of our mass spectrometer, no measurements were conducted from 22 March to 14 April. During the summer (June to August), the observation data behaviour of HFC-134a and HFC-125 suggested a local pollution source in the vicinity (a few 100 m) of the
165   station, assumed to be a leaking refrigeration/air conditioning system close by. Because the transport model (see Section 2.4) cannot account for such local emissions, HFC-125 and HFC-134a data were removed during the summer when local wind speeds were below 4 m s^{-1} and the wind direction was NNE-E.

Since the transport simulations can only account for the regional emissions in a limited domain
and during the time of backward integration, it was necessary to obtain a baseline mole fraction
that represents the conditions at the endpoints of the transport simulation. To this end, a statistical method was applied to the observations assuming that a considerable part of the observations was not, or only weakly, influenced by emissions within the period of the transport simulation. The "Robust Estimation of Baseline Signal" (REBS) algorithm [*Ruckstuhl, et al.*, 2012] detects these baseline observations by iteratively fitting a local linear regression model to the data, excluding data points outside a range around the baseline and finally arriving at a smooth baseline curve. The measured dry air mole fraction, X_O, can then be represented as the sum of the baseline mole fraction, $X_{O,b}$, and the input due to recent emissions, $X_{O,E}$.

The REBS method was applied separately to the high frequency observation data of each compound and each observation site, using a temporal window width of 30 days and a maximum of 10 iterations with asymmetric robustness weights. Derived mean baseline values for each site and the respective baseline uncertainties, σ_b, are shown in SI-Table 1. Finally, three-hourly aggregates were produced from the observations at Finokalia and the other European AGAGE sites (JFJ, MHD, CMN) in order to match the transport model's temporal output interval.

2.4 Transport Simulations

The Lagrangian Particle Dispersion Model FLEXPART (version 9.02) [*Stohl, et al.*, 2005] was used to derive source sensitivities, also referred to as footprints, for 3-hourly intervals at all four observational sites. The source sensitivities quantify the effect of an emission source at a certain grid location and of unit strength (1 kg s^{-1}) on the mole fractions at the receptor. Multiplication of the source sensitivity with an emission field and summation over the entire grid yields the simulated mole fraction at the receptor [*Seibert and Frank*, 2004; *Stohl, et al.*, 2009]. FLEXPART calculates transport by mean and turbulent flow as well as transport within convective clouds. Here, it was driven by meteorological fields obtained from the operational analysis of the Integrated Forecast System (IFS), provided by the European Centre for Medium-Range Weather Forecasts (ECMWF). Input fields were available at 3-hourly intervals at a global resolution of 1° by 1° and a nested domain with a resolution of 0.2° by 0.2° for the Alpine area. FLEXPART was run in "backward" mode, where 50'000 particles were released from each observation site in 3-hourly intervals and followed 10 days backward in time. Assuming that emissions are predominantly originating at the ground, the source sensitivities were calculated for a layer reaching from 0 m to 100m above ground. According to the experience of

previous studies, the release height of particles, followed by FLEXPART along backward tra-
jectories, was set to 3000 m a.s.l. and 2000 m a.s.l. for the high-altitude stations JFJ and CMN,
respectively, where model and real topography differ significantly [*Keller, et al.*, 2012]. For
Finokalia, a particle release height of 150 m a.s.l., corresponding to 30 m above the model
205   topography, was chosen, 70 m below the real altitude. However, a comparison between this
release height and a release at the true altitude above sea level did not show any significant
differences.

Because of the long lifetime of the substances analysed in this study, removal processes were
neglected in the FLEXPART simulations. Of the analysed compounds, HFC-152a has the short-
210   est tropospheric lifetime of 1.6 years [*Carpenter and Reimann*, 2014]. Applying this average
lifetime, only about 1.7 % of fresh HFC-152a emissions would be degraded during the 10-day
transport period.

2.5   Atmospheric Inversion

To estimate spatially resolved emissions, a Bayesian inversion method [*Enting*, 2002] as im-
215   plemented and described in *Henne et al.* [2016] was used. Here we only describe the most
integral parts of the method and modifications as compared with *Henne et al.* [2016].

In short, the source sensitivities simulated by FLEXPART provide the link to describe a linear
relationship between simulated mole fractions at the observation sites, y, and an emission field,
x, which can be written in matrix notation as

$$y = \boldsymbol{M}x, \tag{1}$$

220   where $\boldsymbol{M}$ is the source sensitivity matrix constructed from the individual source sensitivities.
The state vector, x, contains the emissions of each grid cell in the inversion grid and baseline
mole fractions, given at baseline nodes at discrete time intervals for each site. Consequently,
the matrix $\boldsymbol{M}$ contains two block matrices $\boldsymbol{M}^E$ and $\boldsymbol{M}^B$, denoting the dependence on emissions
and baseline mole fractions, respectively. $\boldsymbol{M}^B$ is designed such that the elements represent tem-
225   porally linear interpolated values between neighbouring baseline nodes [*Stohl, et al.*, 2009;
Henne, et al., 2016].

In the Bayesian approach, the a posteriori state, x_{post}, is obtained such that the simulations
optimally fit the observations, y_O, under the presumption of a given prior state x_{prior}. This can
be achieved by the minimization of the following cost function,

$$J = \frac{1}{2}\left(x_{post} - x_{prior}\right)^T B^{-1}\left(x_{post} - x_{prior}\right)$$
$$+ \frac{1}{2}\left(Mx_{post} - y_0\right)R^{-1}\left(Mx_{post} - y_0\right),$$

(2)

230 where the first term gives the deviation of the posterior state vector x_{post} from the a priori state
vector x_{prior} and the second term, the misfit between the simulated mole fractions, Mx_{post},
and the observations, y_O. B is the uncertainty covariance matrix of the a priori state vector and
R denotes the uncertainty covariance matrix of the data-mismatch and contains both observa-
tion and model uncertainties. Section *Covariance Treatment* details how B and R were set up

235 for this study. The diagonal elements of the uncertainty covariance matrix are hereinafter re-
ferred to as "analytic uncertainty".

To increase the spatial coverage of our analysis and thereby reduce the uncertainties at the
periphery of the Eastern Mediterranean, simultaneous measurements from the three AGAGE
sites in Western Europe were included in addition to those at Finokalia. Thus, our inversion

240 grid covered most of Southern and Central Europe, reaching from the Atlantic to the Middle
East. To represent the large variety of advection patterns, influencing the observations at the
AGAGE sites in our study area, measurements from Dec. 2012 – Dec. 2013 were used in the
inversion.

The applied inversion derives spatially-resolved, but temporally-constant emissions. In order to

245 reduce the size of the inverse problem, which depends on the number of grid cells, an inversion
grid with variable grid resolution was defined. Grid cells, for which the average source sensi-
tivity was below a predefined threshold were joined with their neighbours until the combined
source sensitivity was sufficiently large or up to a maximum horizontal grid size of 6.4° by
6.4°. In contrast to previous studies, using variable grid resolutions [*Stohl, et al.*, 2009; *Brunner,*

250 *et al.*, 2012a; *Henne, et al.*, 2016], the initially computed irregular grid was manually adjusted
to ensure that large grid cells did not overlap with different emission regions. This assured a
more accurate assignment of emissions per region and their uncertainties, especially in the case
of large emissions close to regional borders, and when different a priori uncertainties were given
to neighbouring regions.

255 ## 2.6 A priori Emissions

A Bayesian inversion requires a priori knowledge of the state vector to guide the optimisation
process. In order to specify a priori emissions and their uncertainty for each grid cell of the

inversion grid, emission information was collected on the country/region level and then spatially disaggregated following population density. Since optimising emissions from small and

260 distant (from the observation locations) countries can be afflicted with large uncertainties, we aggregated country-specific a priori information to larger regions (see Table 3 and SI-Figure 2). These were introduced with the intention to separate developed (Annex I/ Non Article 5) and developing (Non Annex I/ Article 5) countries wherever possible. Total a priori uncertainties were assigned to each country/region and each compound separately and then spatially

265 disaggregated following the same population density as for the emissions, which results in constant relative uncertainties for each country/region. This is an improvement as compared with previous studies that used uniform relative uncertainty in the whole inversion domain. [e.g., *Keller, et al.*, 2012].

Our a priori country total HFC emissions for Annex I parties were based on the 2016 National

270 Inventory Submissions to the UNFCCC [*UNFCCC*, 2016] for the year 2013, collected from individual country "common reporting format" tables. To estimate prior emissions for countries within our inversion domain not reporting to the UNFCCC (Non-Annex I), reported emissions were subtracted from estimated global emissions in 2012 provided by *Carpenter and Reimann* [2014]. The remaining emissions were further disaggregated to the individual country level,

275 based on population data, provided by the UN population division [*UN*, 2016]. Uncertainties for reported "bottom-up" emissions were arbitrarily set to 20%, whereas estimated a priori emissions for non-reporting countries were given a higher uncertainty of 100% (Table 3). The sensitivity of our posterior emissions to these choices was analysed in additional inversion runs (see Section 2.8).

280 HCFC-22 global emission estimates provided by *Carpenter and Reimann* [2014] were distributed based on regionally estimated shares by *Saikawa et al.* [2012], assuming that contribution ratios of the regions defined in their study have not changed significantly since the period of 2005 – 2009. Emission estimates in areas with differing regional extents in our study compared to that of *Saikawa et al.* [2012] were rearranged using population data. The resulting prior emis-

285 sions for the European domain compare well with estimated European emissions, derived by *Keller et al.* [2012] during their campaign in 2011. Uncertainties were calculated to add up to a combined uncertainty of the used global estimate from *Carpenter and Reimann* [2014] and the regional estimates derived by *Saikawa et al.* [2012] (Table 5.5).

Based on the assumption that HCFC-142b and HCFC-22 emissions are largely collocated, the

290 same above mentioned regional emission shares are used to derive HCFC-142b prior emissions.

Resulting European emissions were further scaled to match HCFC-142b estimates from *Keller et al.* [2012], while Russian emissions, which were not covered in the above mentioned study, were scaled using temporally extrapolated emissions from EDGAR [*JRC/PBL*, 2009]. Due to the lack of information and on the basis that Article 5 countries are still allowed to use HCFCs

295   after the phase-out of HCFCs in non-Article 5 countries, North African and Middle Eastern countries within our domain were left unscaled, but given a regional total uncertainty of 100% allowing for substantial corrections of the a priori emissions by the inversion. European regions containing developing and developed countries, as well as Russia were assigned a smaller uncertainty of 50%, reflecting the availability of scaling information.

300   ## 2.7   Covariance Treatment

We followed three different strategies how to design the covariance matrices $\boldsymbol{B}$ and $\boldsymbol{R}$. The first two ('Global' and 'Local') use complete uncertainty covariance matrices and are similar to the one used in *Henne et al.* [2016], whereas the third method ('Stohl') assumes uncorrelated uncertainties and uses diagonal-only uncertainty covariance matrices [*Stohl, et al.*, 2009]. The

305   latter has already been used successfully to derive regional halocarbon emissions [e.g. *Vollmer, et al.*, 2009; *Keller, et al.*, 2012].

The uncertainty covariance matrix $\boldsymbol{B}$ of the a priori state-vector consists of two symmetric block matrices $\boldsymbol{B}^E$ and $\boldsymbol{B}^B$, containing the uncertainty covariance of the gridded a priori emissions and the baseline mole fractions, respectively. Diagonal elements of $\boldsymbol{B}^E$, defining the uncertainty

310   of each grid cell emission, were set proportional to the a priori emissions in each cell. The diagonal elements of $\boldsymbol{B}^B$ were set to the constant value of the baseline uncertainty σ_b, as estimated by the REBS method for each observation site (see Section 2.3), scaled by a constant factor f_b. For the covariance methods 'Global' and 'Local' the off-diagonal elements of $\boldsymbol{B}^E$ were defined according to a spatial correlation, decaying exponentially with the distance be-

315   tween a grid cell pair and utilising a correlation length, L, which was set to 200 km for all inversions. Furthermore, the baseline mole fractions were assumed to be correlated temporally, described by an exponentially decaying relationship in the off-diagonal elements of $\boldsymbol{B}^B$, based on the temporal correlation length, τ_b, set to 5 days. For the covariance method 'Stohl', $\boldsymbol{B}$ only contained values in the diagonal, implying uncorrelated a priori uncertainties. For all three ap-

320   proaches, it was assured that the total by-region a priori uncertainty of emissions is the same as defined above.

The covariance matrix $\boldsymbol{R}$ contains the uncertainty of the observations and the model (data-mismatch), $\sigma_c = \sqrt{\sigma_O^2 + \sigma_{model}^2}$. For the covariance methods 'Global' and 'Local' the diagonal elements of $\boldsymbol{R}$ were defined as a combination of the observation uncertainty σ_O and the model

325   uncertainties σ_{model}. σ_O contained the measurement uncertainty (see Section 2.2) and σ_{model} was calculated iteratively for each site, incorporating the root mean square error (RMSE) between an a priori simulation and the observed mole fractions. Off-diagonal elements of $\boldsymbol{R}$ were assumed to follow an exponentially decaying structure [*Henne, et al.*, 2016]. The temporal correlation length, τ_C, of the combined uncertainty, σ_c, was based on the autocorrelation of the a

330   priori model residuals. Two different approaches were followed to determine τ_C. First (method 'Global'), a constant value of τ_C for the entire time period and each site was estimated fitting an exponential decay to the first two lags of the global autocorrelation function of the residuals. In a second approach ('Local'), the autocorrelation was evaluated locally within moving windows with a half-width of 80 data points (10 days). Again, τ_C was then calculated from an

335   exponential fit to the first three values of the autocorrelation function for each window. These procedures to estimate τ_C worked successfully for all compounds and sites, except for HFC-143a at Finokalia, for which large, unexplained peaks in the observed time series lead to very large values in the autocorrelation function and consequently τ_C. To allow for a meaningful inverse adjustment, a constant τ_C was used for HFC-143a, based on the mean value of τ_C for

340   the other compounds.

In the alternative approach ('Stohl') $\boldsymbol{R}$ was specified similar to the above-mentioned method, using the RMSE between a priori simulation and observations. In addition, the extreme values in the residual distribution were filtered and assigned larger uncertainties, in order to derive a more Gaussian distribution of the a priori residuals normalised by σ_C [*Stohl, et al.*, 2009]. As a

345   result, a disproportional influence of extreme values, which were not resolved well by the transport model, can be avoided. Furthermore, off-diagonal elements in $\boldsymbol{R}$ were set to zero in this approach.

2.8   Sensitivity Inversions

The a posteriori uncertainty, analytically estimated by a Bayesian inversion, often strongly de-

350   pends on assumptions made on the a priori and data-mismatch uncertainty as well as on the general design of the inversion system. A number of previous studies have shown that this analytical uncertainty is often too small to realistically cover the real a posteriori uncertainty [e.g., *Bergamaschi, et al.*, 2015]. To further explore the range of this structural uncertainty of

the inversion setup and test the robustness of the a posteriori results, a set of sensitivity inversions were performed (Table 1).

The inversion using the a priori emissions as described above, the 'Global' method for setting up the covariance matrices **B** and **R**, and observations from all four sites was chosen to represent the base inversion (BASE) setup. The base case does not necessarily offer the best inversion settings for each substance and each site, as these are generally not known, but serves as a starting point to assess the sensitivity of the inversion towards differently chosen parameters.

A first set of sensitivity inversions was used to analyse the effect of different covariance matrix designs. In contrast to the BASE inversion, S-ML and S-MS used the 'Local' and 'Stohl' approach as described in Section *Covariance Treatment*.

We then explored the sensitivity of our a posteriori results towards a priori emission uncertainties, with regard to the inhomogeneous availability of a priori information on halocarbon emissions within our inversion grid. To this end, the a priori uncertainty for each region was increased/decreased by 50 % as compared to the base uncertainty (S-UH, S-UL).

In a third set of sensitivity runs the influence of the additional observations gathered during the campaign at Finokalia on the a posteriori emissions in western Europe, central Europe and the Eastern Mediterranean was tested. One sensitivity inversion was set up, excluding the observations from Finokalia (S-NFKL), whereas in a second inversion, only measurements from Finokalia were taken into account (S-OFKL). Using this approach, two questions can be answered. First, what is the gain of the Finokalia observations for top-down emission estimation in the Eastern Mediterranean and, second, did the inclusion of the additional AGAGE sites provide substantial constraints for the same area?

3 Results and Discussion

In this section, an overview about the measurements taken in Finokalia (FKL) is followed by a comprehensive presentation and discussion of the inversion results. The performance of the BASE inversion is shown exemplarily for HFC-134a in more detail before the results of the sensitivity inversions are presented, highlighting the differences between the BASE case and these inversions. The "top-down" emission estimates for defined regions within the inversion domain are shown in the last section.

3.1 Flow Regime and Observations at Finokalia

During our measurement campaign from December 2012 to August 2013, local wind observa-
385   tions showed a transition from a northerly wind regime in December to a more variable wind
regime with a bias towards westerly directions from January to June. July and August were
characterized by very constant easterly to north-easterly winds. These local observations agree
with the results of the atmospheric transport simulations, showing air transported to the station
from the African continent and the Western Mediterranean in February and March (Figure 2a).
390   The area of influence changes more towards South-eastern Europe in early summer, whereas in
July and August, air is transported from a narrowly defined north-easterly sector (Figure 2b).

These conditions observed during the campaign in 2012/2013 agree with previous descriptions
of the wind climatology at FKL that also observed two distinct meteorological regimes in Crete.
During the dry season from May to September, air masses are usually advected from central
395   and eastern Europe and the Balkans, whereas the wet season from October to April is more
variable in terms of air transport and favours air masses from the African continent and from
marine influenced westerly sectors [*Kouvarakis, et al.*, 2000; *Gerasopoulos, et al.*, 2005].
Therefore, the halocarbon observations presented here can be expected to be the result of typical
advection conditions at FKL.

400   The halocarbon observations collected at FKL during the campaign are shown in Figure 3,
together with data from JFJ and CMN for comparison. The range of the observations at FKL
and the temporal evolution of the atmospheric baseline signals agreed well between the sites.

For HFC-134a and HFC-125, which are mainly used as refrigerants in mobile and stationary
air conditioning, the maximum measured mole fractions and the variability at FKL was smaller
405   than what was simultaneously measured at the two other stations. This could be expected from
the maritime influence at FKL, with the closest larger metropolitan areas at a distance of 350-
700 km, as compared to nearby emission hot-spots for JFJ and CMN (e.g., Po Valley). For
HFC-143a, pollution peaks were comparable to the measurements at CMN during a short period
in the beginning of the campaign (Dec - Feb). After this period, the variability decreased with
410   no more large pollution peaks observed. HFC-152a and HCFC-22 observations showed a sim-
ilar pattern at FKL as at the other sites. Particularly high mole fractions during several pollution
periods were observed for HCFC-22, indicating the proximity of emissions possibly from Ar-
ticle 5 countries where the use of HCFCs has just recently been capped. Although the highest-
observed mole fractions were relatively large, they occurred less frequently than those observed

415   at JFJ and CMN. This was probably due to distant but strong pollution sources influencing the observations at FKL. HCFC-142b mole fractions showed large variability and comparably large peak mole fractions during the summer period at FKL, but again with a slightly lower frequency than at JFJ.

The mean baseline values at FKL for HFC-134a, HFC-125, HCFC-22 and HCFC-142b, calcu-
420   lated with the REBS method [*Ruckstuhl, et al.*, 2012], were within a range of ±7 % of the baseline values derived for the other three sites (see SI-Table 1). Maximum baseline deviations of ±13 % were estimated for HFC-143a and HFC-152a as compared with JFJ.

3.2   Base Inversion

For the BASE inversion, the covariance design based on the 'Global' autocorrelation function,
425   as described in Section *Covariance Treatment*, was used, combined with the complete set of observations from all four sites, including the observations from FKL. Exemplarily, a comparison of simulated prior and posterior HFC-134a with the underlying observations is shown in Figure 4. At all four sites, the simulated a priori mole fractions reproduced the variability of the observations, indicating satisfactory performance of the transport model. Simulations of the a
430   priori mole fractions showed a tendency to underestimate the observations during peak periods at JFJ, MHD, and CMN, whereas the a priori simulation generally overestimated the observations at FKL. Here, a similar behaviour of the a priori simulations was also observed for HFC-152a, whereas the tendency to underestimate the observations (like at the AGAGE sites) was apparent for all other analysed compounds. Since FKL and the AGAGE sites are mostly sensi-
435   tive to distinctly different regions, the general overestimation in the prior simulations already points towards generally overestimated or spatially misallocated a priori emissions in the Eastern Mediterranean.

For all four stations, the inversion considerably improved the correlation between observations and simulations, which was evaluated based on the coefficient of determination R^2. The perfor-
440   mance of the simulated a posteriori signal increased to $R^2 = 0.74$ for FKL and MHD, 0.5 for JFJ and 0.54 for CMN, which corresponds to an improvement of R^2 by $\Delta R^2 = 0.33$ for FKL, $\Delta R^2 = 0.13$ for MHD, $\Delta R^2 = 0.17$ for JFJ and $\Delta R^2 = 0.15$ for CMN (Table 2). Only accounting for the simulated and observed signal above the baseline, the performance was lower for FKL ($R^2 = 0.29$), JFJ ($R^2 = 0.34$) and CMN ($R^2 = 0.28$). The correlation of the signal above the
445   baseline for MHD ($R^2 = 0.73$) remains as high as for the complete signal. These values indicate good inversion performance results and are comparable to other studies, using similar inversion

schemes [*Stohl, et al.*, 2009; *Vollmer, et al.*, 2009; *Keller, et al.*, 2012]. The performance ranking between the sites and the large above baseline correlation at MHD also agree with our expectations. The latter is due to the coastal location of MHD with negligible emissions west of

450   the site for several thousand kilometres across the Atlantic Ocean and the fact that synoptic scale flow, which is well captured by the transport model, intermittently drives European emissions towards the site. In contrast, transport to JFJ and CMN is driven by small scale flow systems and baseline conditions are generally less well-defined in free tropospheric conditions that tend to be more variable. Finally, while FKL is a coastal site like MHD, it does not exhibit

455   a well-defined baseline sector, since emission sources may be found at the entire coastline in the Eastern Mediterranean at distances around 1000 km from the site.

To evaluate the ability of the model to simulate the observed amplitudes correctly, we used the Taylor skill score (TSS), combining correlation and variability of observed and simulated mole fractions [*Taylor*, 2001]. The maximum attainable Pearson correlation coefficient, indicating a

460   "perfect" simulation in terms of the strength of the relationship between simulated values and observations, was set to 0.9. Thus, a TSS of 1 indicates a perfect simulation with regards to amplitude and correlation, whereas a TSS of 0.65 means that the observed variability is under/overestimated by a factor of 2 for perfectly correlated simulations. Although the normalized standard deviation decreased for FKL, the TSS was increased to 0.95 due to the improvement

465   of the correlation of posterior results and observations, indicating, that although the relationship of observations and simulations was increased, the inversion did not adjust the amplitudes of the pollution peaks. At CMN the a posteriori TSS increased to 0.74, driven by both, an increase of the normalised standard deviation and correlation, whereas the TSS for JFJ and MHD decreased to 0.71 and 0.75 respectively. The latter is due to a reduction of simulated peak heights

470   compared to the a priori simulation, while the correlation was strongly improved. In general, the resulting Taylor skill scores were in a similar range as in previous regional-scale inversion studies [*Brunner, et al.*, 2016; *Henne, et al.*, 2016].

Model and inversion performance were also evaluated using the Root-Mean-Square-Error (RMSE; a combined measure of variability and bias) between simulated and observed mole

475   fractions. Its reduction from a priori to a posteriori simulations amounted to 20%, 12% and 10% for JFJ, MHD and CMN, respectively. The absolute a posteriori RMSE was in the range of 2.9 – 5 ppt for these sites. The RMSE improvement for FKL from the a priori RMSE (4.7 ppt) to the a posteriori RMSE (1.7 ppt) was much larger (64%). This can be attributed to the above-mentioned overestimation of the simulated prior values and the optimisation by the inversion,

480 which also included a considerable reduction of the baseline. Again, these RMSE reductions were in a similar range as those reported in previous studies [*Stohl, et al.*, 2009; *Vollmer, et al.*, 2009; *Keller, et al.*, 2012].

The inversion performance of HFC-125 and HCFC-142b was similar to HFC-134a, with mean posterior TSS of 0.81 and 0.78, respectively, compared to 0.78 for HFC-134a. For HFC-152a,
485 HFC-143a and HCFC-22 they decreased to 0.73, 0.74 and 0.75, respectively (Table 2).

For the BASE inversion of the exemplary compound HFC-134a a posteriori were mostly smaller than a priori emissions with the exception of areas in Northern Italy, Slovenia, Croatia and along the western part of the British Channel (Figure 5). Most pronounced emission differences in the Eastern Mediterranean were associated with the larger urban centres in Greece and
490 Turkey (Athens, Thessaloniki, Istanbul), whereas in Western and Central Europe similarly large reductions were assigned to the Benelux area and the western part of Germany as well as to the UK. Within the same BASE inversion of HFC-134a the analytic uncertainty in the Eastern Mediterranean was reduced by more than 80% from its prior value for grid cells containing large metropolitan areas such as Athens and even Cairo (Figure 5). For Western Turkey and
495 large parts of the Balkans, the uncertainty was reduced by 30-60%, which shows, that we achieve satisfactory emission estimates for the targeted areas in the Eastern Mediterranean. Similar reductions are also achieved over large parts of Western and Central Europe, to which the AGAGE sites are sensitive. Although other adjacent areas such as Middle Eastern countries bordering the Mediterranean Sea (e.g., Israel, Jordan) and countries further Northeast (e.g.,
500 Ukraine) were detected during our measurement campaign, the uncertainty was reduced less by the inversion (10-30%).

Similar patterns of uncertainty reduction resulted for HFC-152a, HFC-125, HCFC-22 and HCFC-142b. For HCFC-142b, the reduction was lower for the Balkans (~ 10%), but similarly large for Western Turkey (20-40%). For HFC-143a, the uncertainty was reduced by 20 % for
505 the area of Athens, whereas only negligible reductions were estimated for Turkey.

3.3 Sensitivity Inversions

3.3.1 Influence of Covariance Design

The first sensitivity inversion, S-ML, uses the 'Local' approach to estimate the temporal correlation length scale of the data-mismatch uncertainty (see Section 2.7). As a consequence, the

weights different observations were given in the inversion were slightly redistributed as compared with the BASE inversion. For our exemplary compound HFC-134a, the model performance in terms of the RMSE was similar to the BASE inversion at FKL, CMN and JFJ. For MHD the RMSE was not reduced by the inversion, thus, compared to the base inversion, posterior RMSE values were 14% higher. The same pattern was observed for the coefficient of determination R^2, which was increased by less than 2% for FKL, CMN and JFJ, but dropped by approximately 8% at MHD. Despite the slight increase in the correlation at FKL, CMN and JFJ, the Taylor Skill Score decreased between 1-4%, indicating that in the S-ML case, the peak amplitudes are not as well simulated as in our BASE inversion. For MHD, the TSS was reduced by 12%, reflecting that in addition to the lower correlation, S-ML also underestimated the peak amplitudes at this coastal location.

The sensitivity case S-MS used uncorrelated a priori and data-mismatch uncertainties (see Section 2.7). As opposed to S-ML, the RMSE of S-MS for HFC-134a was improved by 14%, 6% and 2% at MHD, JFJ and CMN respectively, as compared with the BASE inversion, whereas no improvement was observed for FKL, which showed a small RMSE of 1.7 ppt in the BASE inversion already (SI-Table 2). R^2 was generally higher for S-MS compared to the BASE inversion. It increased between 1-3% for FKL, CMN and MHD and by 6% for JFJ, showing the best absolute performance for MHD and FKL in the posterior R^2, with 0.76 and 0.75, respectively. As indicated by higher Taylor skill scores (SI-Table 2), S-MS was also able to more closely reproduce the amplitude of the peaks at all sites as compared with the BASE inversion.

Total HFC-134a emissions for the whole inversion domain were 10% lower for the S-ML case, whereas they were 30% higher for S-MS, as compared to the BASE inversion. While regional emissions from Greece and the Balkans were relatively unaffected in the S-ML case, more pronounced negative deviations compared to BASE were established for Turkey (-14%), Central W (FR, LU, NL, BE; -23%) and the Iberian Peninsula (ESP, PT; -22%) (Figure 5 and Figure 6b,c). A posteriori differences were less smooth in the S-MS inversion as compared to the BASE and S-ML inversions (Figure 6), reflecting the effect of not using a spatial correlation in the a priori emissions. Regional emissions estimated with S-MS were generally higher as compared to the base inversion (Figure 6c). Significantly (40%, $p < 0.05$) higher emissions were obtained in the UK and Ireland compared to the BASE inversion. Regional emissions of North-Western Europe and the Balkans were larger by 20-60% in S-MS.

In summary, S-ML showed a slightly weaker performance than the BASE inversion, with insignificantly lower total emission estimates but similar analytic uncertainties. On a regional

level, the impact of S-ML on the estimated emissions varies by region, showing less influence on the Balkans and Central W, whereas larger deviations were seen for Turkey, Western and the British Isles. On the contrary, S-MS performed slightly better and resulted in generally larger emissions than the BASE inversion, but confirmed the significant emission reductions as compared to the a priori emissions.

3.3.2 Influence of A Priori Uncertainty

To assess the influence of our regionally assigned a priori uncertainties, the sensitivity inversions S-UL and S-UH were run with 50% smaller and larger a priori emission uncertainties as compared to the base inversion. As expected, a posteriori model performance generally increased with larger a priori uncertainties because the optimisation is less constrained by the prior. However, HFC-134a domain total a posteriori emissions remained similar to those in the BASE inversion, whereas S-UL resulted in slightly increased emission estimates, remaining closer to the prior emissions (see supplement). A posteriori HFC-134a emission uncertainties were decreased (increased) by ~28% and ~16% in comparison to the BASE inversion, if a priori emission uncertainties were smaller and larger, respectively (SI-Figure 3).

In general, the absolute emission estimates for the study domain seemed to be very robust to changes in the a priori uncertainty. A posteriori emission estimates for the case with lower a priori uncertainties (S-UL), comprising all the analysed species except HFC-134a, showed insignificantly larger total emissions. This reflects the constraint, which requires the results to follow the a priori emissions more closely in this case. Total a posteriori emissions in the case of larger a priori emission uncertainties remained close to our BASE case. Emission uncertainties in the a posteriori, as compared to the BASE inversion, were on average about 18% higher and 27 % lower for the S-UH case and the S-UL case, respectively. This tendency can be expected from the a priori emission uncertainties. The results of these two sensitivity inversions emphasize the general robustness of the inversion system to changes in the a priori emission uncertainties. Exceptions in the case of HFC-134a are discussed in the following section.

3.4 Regional Total Emissions

Our estimated regional total emissions are summarized in Table 3 and Figure 7. The "top-down" emission estimates presented here are the mean values of the BASE and four sensitivity inversions (S-ML, S-MS, S-UH, S-UL). The uncertainty range given here and in Table 3 represents the range of these five inversions based on their mean values and the analytical a posteriori

uncertainty (95% confidence interval), whichever is larger. This measure was chosen to accom-
modate, on the one hand, the analytical uncertainty as estimated by the Bayesian formulation
and estimated for each inversion run as the a posteriori uncertainty, and, on the other hand, the
structural uncertainty that is reflected by the spread of the sensitivity inversions and results from
choices in the parameter selection of the covariance design. The comparison between structural
and analytic uncertainties reveals that the dominating type of uncertainty varies largely between
different compounds and different regions. For most compounds and regions, the two types of
uncertainty fall within a similar range (HFC-152a; HFC-143a; HFC-125; HCFC-22; HFC-134a
only in the eastern part of the domain). For HCFC-142b the structural uncertainty was generally
smaller than the average a posteriori uncertainty. In contrast, for HFC-134a and the western
part of the domain (British Isles, Iberian Peninsula, Western, Central W) the structural uncer-
tainty was clearly larger than the analytical uncertainty.

This relatively large spread in the sensitivity inversions results from the differences between
the sensitivity inversions with different covariance matrices (S-ML and S-MS), where a general
tendency to smaller changes from the a priori (resulting in larger a posteriori emission) was
observed for the western part of the domain and for Turkey. In addition, a similar tendency was
observed for the same regions, except the Western region, when different a priori uncertainties
were applied (S-UH, S-UL, SI-Figure 3). Therefore, combining the results from all sensitivity
inversions revealed relatively large uncertainties in the "top-down" estimates in a region that is
relatively well covered by the existing AGAGE network and emphasizes the use of such sensi-
tivity tests to explore the real uncertainty of the "top-down" process and the need for more
objective methods to derive the data-mismatch covariance matrix.

3.4.1 HCFCs

HCFC-22 is the most abundant HCFC in today's atmosphere and has been widely used as a
refrigerant and foam blowing agent in much larger quantities than other HCFCs. Due to regu-
lations by the Montreal Protocol, global emissions have remained constant since 2007
[*Carpenter and Reimann*, 2014]. Our "top-down" emission estimate for the regions listed in
Table 3 (in the following referred to as total emissions) amounted to 9.1 (4.5-14) Gg yr^{-1}. As
expected, high emissions were concentrated in regions, defined by the Montreal Protocol as
developing (Article 5) countries, such as Egypt, the Middle East and Turkey, accounting for
43% (22-67%) of the total emissions. Our estimates for Central and Western European (regions
Western, Central W, British Isles, Iberian Peninsula and Italy) emissions are 3.1 (2.0-4.3) Gg yr^{-}
^{1}, which is 69% (57-81%) less than reported by *Keller et al.* [2012] for the same area in 2009,

suggesting that HCFC-22 emissions continue to decrease in these developed countries. How-
ever, major pollution events were observed at FKL when air arrived from areas such as Egypt,
which may be explained by the fact that caps to HCFC production and consumption for Article

610 5 parties began only in 2013. For the total domain, our a posteriori estimates were significantly
lower than the a priori values. On the regional scale, a posteriori estimates were larger than a
priori for the above-mentioned Article-5 countries (Egypt, Middle East), whereas this tendency
was inversed for Non-Article 5 countries. These results agree with the expectation that due to
the stepwise phase out of HCFCs in developing countries and the inherent time lag until release

615 to the atmosphere [*Montzka, et al.*, 2015], HCFC-22 emissions remain at considerably high
levels.

HCFC-142b is applied mainly as a foam blowing agent for extruded polystyrene boards and as
a replacement for CFC-12 in refrigeration applications [*Derwent, et al.*, 2007]. Our total esti-
mated emissions sum up to 1.0 (0.5-1.6) Gg yr^{-1}. Turkey, listed as an Article 5 party, accounts

620 for 13.8% (4.7-23.0%) of these total emissions, whereas the contribution of other Article 5
regions is less pronounced as compared to HCFC-22. Average a posteriori emissions in the
Eastern Mediterranean (regions Greece, Turkey, Middle East, Egypt, Balkans and Eastern) are
estimated to 0.40 (0.09-0.74) Gg yr^{-1}, which is about half of the domain total emissions. How-
ever, our inversion was not able to significantly reduce the uncertainty estimate for these re-

625 gions, demonstrating the need for additional and continuous halocarbon measurements in this
area. HCFC-142b emissions in Central and Western Europe, where the use of HCFCs has prac-
tically been phased out, show a comparatively large contribution of 0.53 (0.39-0.67) Gg yr^{-1},
which accounts for 39.7% (31.3-48.5%) of the domain total emissions. Although the spatial
distribution of HCFC-142b emissions in Central Europe resembles the pattern derived by *Keller*

630 *et al.* [2012], dating back to emissions from 2009, our estimates indicate a reduction by a factor
of ~2. Our estimates are also lower by the same factor ~2 compared to bottom-up estimates of
HCFC-142b emissions, as reported in EDGARv42 [*JRC/PBL*, 2009] for the year 2008, for both
Western Europe and the Eastern Mediterranean. However, the latter is mainly driven by gener-
ally smaller emissions in the Eastern and Balkan regions, whereas for Turkey, the Middle East

635 and Egypt larger than EDGAR values were estimated by the inversion. The general decrease
within the domain is in line with global emissions of HCFC-142b, which are considerably lower
than those of HCFC-22 and have declined by 27%, from 39 (34-44) Gg yr^{-1} to 29 (23-34) Gg yr^{-1}
between 2008 and 2012 [*Carpenter and Reimann*, 2014; *Montzka, et al.*, 2015]. The compar-
ison of a priori and a posteriori emissions of HCFC-142b shows a much more diversified pattern

640   than for HCFC-22, with regions such as Turkey and Western E, where our bottom-up assumptions were too low, whereas they were too high for Maghreb and Egypt and agreed well for Italy, Greece and Central W.

3.4.2   HFCs

HFC-134a is currently the preferred refrigerant in mobile air conditioning systems and, together

645   with HFC-125, which is mostly used in refrigerant blends for residential and commercial refrigeration, belongs to the two most popular HFCs in Europe [*O'Doherty, et al.*, 2004; *O'Doherty, et al.*, 2009; *Velders, et al.*, 2009; *Xiang, et al.*, 2014]. This is reflected by the large amplitude and frequency of pollution peaks, which were observed at all continuous observations sites but especially at JFJ and CMN (Figure 3). Total simulated HFC-134a emissions for

650   our analysed regions were 19.0 (13.3-25.8) Gg yr^{-1}. Emissions from Eastern Mediterranean (Greece, Turkey, Balkans, Eastern, Middle East, Egypt) summed up to 4.6 (2.5-6.9) Gg yr^{-1}, which is ~24% of the domain total emission. The remaining 63% were emitted from Central and Western Europe, totalling at 11.9 (9.4-15.2) Gg yr^{-1}. Comparing the aggregated emissions of reporting regions to UNFCCC inventories reveals that the inversion generally estimated a

655   posteriori emissions of HFC-134a that were 47.5% (32.0-60.3%) lower than the respective UNFCCC reports. Only HFC-134a emissions of Italy and Eastern European countries were within the range of reported UNFCCC estimates. Furthermore, our results suggest lower emission in most region in comparison to EDGARv42_FT2010 [*JRC/PBL*, 2009] for the year 2010, with the exception of Greece, Turkey and the Eastern region, where both estimates are very similar,

660   and of Egypt and the Maghreb region, where the inversely estimated emissions were considerably larger than EDGAR values.

These findings of generally smaller than reported HFC-134a emissions in Western and Central Europe resemble the results of other studies performed for earlier years [*Lunt, et al.*, 2015; *Brunner, et al.*, 2016; *Say, et al.*, 2016]. The differences between the country-wide emissions

665   reported to UNFCCC and the range of results found in this study seem to be somewhat more pronounced than in previous studies. This is consistent with *Brunner et al.* [2016], who reported a relatively large range of regional emission estimates depending on the employed inverse modelling system.

HFC-125 domain-total emissions were estimated at 8.1 (6.1-10.3) Gg yr^{-1} with emissions from

670   the Eastern Mediterranean contributing 15 % or 1.2 (0.5 – 2.0) Gg yr^{-1}. Our results for Turkey

agree well with those reported to UNFCCC, but are three times smaller than ED-GARv42_FT2000. For Greece, our estimate of 0.25 (0.19-0.31) Gg yr⁻¹ falls between the much larger UNFCCC value of 0.60 Gg yr⁻¹ and the smaller EDGARv42_FT2010 estimate of 0.1 Gg yr⁻¹. Emissions from the Eastern region, the Middle East and Egypt remained relatively close to the a priori estimates, whereas for the Balkans we derive a 50 % increase compared to the a priori emissions to 0.18 Gg yr⁻¹, which is still considerably smaller than the ED-GARv42_FT2010 value of 0.55 Gg yr⁻¹. This stands in contrast to the results of *Keller et al.* [2012] for the Eastern region, showing large discrepancies between "top-down" and "bottom-up" estimates in some of these countries, most likely caused by unrealistically low values reported to UNFCCC. Besides the fact, that the estimates of *Keller et al.* [2012] rely on measurements from Hungary, with a better coverage of North-Eastern Europe than we have from FKL, the discrepancies would be smaller in a retrospective view, because HFC-125 bottom-up emissions of several Eastern European countries were revised upward in the 2016 submissions to the UNFCCC for the year 2009. The largest part of the remaining HFC-125 emissions (71 %) was allocated to Central and Western Europe by the inversion, and was about 30 % lower as compared to the a priori estimate with the exception of Italy, where a posteriori values were very close to those reported to UNFCCC. Our results for Western and Central Europe broadly agree with those reported by *Brunner et al.* [2016] and *Lunt et al.* [2015]. However, note that *Brunner et al.* [2016] describes a substantial underreporting of HFC-125 emission from the Iberian Peninsula in 2011, whereas we find an overestimation by ~25% for 2013. This has to do with a retrospective revision of the Spanish UNFCCC reporting, which resulted in a doubling of most HFC emissions reported in 2016. In absolute terms, our estimates of 1.5 (1.2-1.8) Gg yr⁻¹ for the year 2013 agrees well with that given in *Brunner et al.* [2016] for the year 2011 (1.1 – 2.8 Gg yr⁻¹).

HFC-143a is another major HFC, which is commonly used in refrigerant blends for stationary air conditioners. It is sparsely used in Eastern European countries (Balkans, Eastern, Greece and Turkey), where our "top-down" estimate showed combined annual emissions of 0.39 (0.20-0.57) Gg yr⁻¹, which corresponds to 6.4% (3.3-9.5%) of the domain total of 6.0 (4.6-7.5) Gg yr⁻¹. Emissions higher than the a priori estimates were determined for Maghreb and Egypt with 0.45 (0.24-0.67) Gg yr⁻¹ and 0.27 (0.09-0.44) Gg yr⁻¹, although relatively large uncertainties are connected with these values, since advection from the respective regions was not often observed. 80% of the HFC-143a emissions within our domain have their origin in Central and Western Europe, with the main sources in the Western region and the Iberian Peninsula. Our

estimates agree within 10% with reported UNFCCC values on the domain total basis. For Turkey and the Eastern region, as well as the Iberian Peninsula and the British Isles, reported values agree closely with our estimates (Δ emission estimates < 7%), whereas our estimates of Central E, Central W, Western, Italy and Greece are 18-35% lower than UNFCCC values.

HFC-152a has the smallest 100-year global warming potential of the major HFCs and is primarily used as foam blowing agent and aerosol propellant. Our domain total "top-down" estimate was 2.8 (1.6-4.5) Gg yr^{-1}, which corresponds to only around 6% of estimated global emissions [*Simmonds, et al.*, 2016]. South-eastern Europe's (Greece, Turkey, Balkans and Eastern) annual emissions were estimated at 1.24 (0.7-2.0) Gg yr^{-1}, corresponding to 44% (26.0-71.2%) of total domain emissions. The largest emissions from any individual region were established for Turkey, 2-3 times higher than our estimates for all other regions within the inversion domain. However, this is still almost a factor of 2 lower than what Turkey reports to the UNFCCC. The UNFCCC inventory of Greece overestimates the posterior emissions inferred in this study by a factor of 5. However, it is known that reporting of this compound is incomplete due to confidentiality considerations, which is why it is likely that the inventories for HFC-152a are incomplete and incorrect. Furthermore, for the UNFCCC, emissions of HFC-152a are reported in the country were the consumer product is manufactured. For example, if a foam is blown in country X and sold to country Y, emissions would mainly occur during usage in country Y but are reported under country X. From a global perspective, this makes sense but is not compatible with real emissions in the respective countries. Emissions from Non-Annex I countries belonging to the Middle East and Northern Africa (Maghreb, Egypt) are small (0.42 (0.03-0.93) Gg yr^{-1}). Our "top-down" estimates for Central and Western Europe make up for the remaining 1.17 (0.84-1.52) Gg yr^{-1} of the annual HFC-152a emissions. For all Central and Western European countries, reporting values to UNFCCC, we find a general tendency, that "top-down" emissions are lower than UNFCCC values, with largest discrepancies for the Iberian Peninsula and Central E. For the British Isles, our results are a factor of 2 smaller than the findings of *Lunt et al.* [2015] for the years 2010-2012. In contrast, our estimates for the British Isles agreed within their uncertainties with those reported in Simmonds et al. [2016], which is also true for our estimates for the Central W region and the Iberian Peninsula. In contrast, our "top-down" estimates for Italy are a factor 2 smaller than reported by the latter authors.

3.5   Summary of Halocarbon Emissions

Our best estimate of domain total halocarbon emissions for 2013 was 85.1 (63.0-109.2) Tg CO$_2$eq yr^{-1} for the four analysed HFCs and 18.3 (9.0-28.2) Tg CO$_2$eq for the two HCFCs. This

corresponds to 12.5% (8.9-16.7%) and 2.6% (1.3-3.9%) of global halocarbon emissions [*Carpenter and Reimann*, 2014]. The HFC emissions from the Eastern Mediterranean (Greece, Turkey, Middle East, Egypt, Eastern, and the Balkans) accounted for 14.7 (6.7-23.3)

740   Tg CO_2eq yr^{-1} and the HCFC emissions from the same region for 9.7 (4.3-15.7) Tg CO_2eq yr^{-1}.

As expected, per-capita CO_2 equivalent emissions of HFCs vary strongly in the Eastern Mediterranean (Figure 8). For Greece, per capita emissions were similar to other Western European countries, whereas for the developing countries (Article 5 countries) in the Eastern Mediterra-

745   nean (Turkey, Middle East), with the exception of Egypt, per-capita HFC emissions were much smaller. On the other hand, per capita CO_2 equivalents of HCFC emissions were largest in Article 5 countries in the Middle East and Maghreb region, where the phase-out of these compounds is delayed as compared to the Non-Article 5 countries in Western Europe. In this context, it is also interesting to note that the HCFC per-capita emissions from Greece (Non-Article

750   5) are similarly large as those from its neighbour Turkey (Article-5).

3.6   Temporal Variability of HFC-152a Emissions

Some of the larger HFC-152a pollution peaks observed at FKL (see Figure 3) are not well reproduced by the transport model. The atmospheric inversion only slightly improved the comparison, indicating the inability to unambiguously assign an emission region or a constant emis-

755   sion process to these peaks. In the following, the transport situations experienced during the observed HFC-152a peaks are analysed in more detail.

The time series of HFC-152a in FKL (Figure 9c) shows intermittently appearing pollution peaks, most pronounced in June and August, which are badly reflected by the simulations, even when a posteriori emissions are used. Especially two observed broader peaks in June and Au-

760   gust are not visible in the simulations. This could be due to inaccuracies in the transport model and weaknesses of the inversion, or because of large, localized, and temporally varying emissions sources, such as HFC-152a production facilities [*Keller, et al.*, 2011]. However, our inversion approach assumes temporally constant emissions and is not able to unambiguously assign a specific source location or area to individually observed pollution peaks that are caused

765   by temporary emissions. For the localization of such emission sources, we used a simple, qualitative approach, by calculating the correlation between the observed HFC-152a time series and FLEXPART simulated source sensitivities in the individual grid cells. First, the correlation for the complete time series was calculated, thereby ignoring the proposed intermittent character

of the source. Using this method, generally positive Pearson correlation coefficients were es-
770   tablished for all land areas with maximal correlation coefficients located in grid cells in North-
western Turkey (Figure 9a). To further isolate the potential source areas, correlations were cal-
culated using only peak periods in the observations at FKL, including the times of increasing
and decreasing mixing ratios at the flanks of each peak. These results showed a further re-
striction of significant positive correlation coefficients to Northwestern Turkey, bordering the
775   Marmara Sea and the Bosporus area (Figure 9b), which are both important industrial regions.
This result could point to large contributions from the metropolitan area of Istanbul, where
HFC-152a could be emitted from installed consumer products. However, due to the strong tem-
poral variability in emissions, which seems to be inherent to the observed peaks, the results are
more likely to be explained with large emissions from an industrial facility in the localized
780   regions.

3.7   The Impact of Halocarbon Observations at Finokalia

Our campaign in Finokalia added halocarbon observations in an area of Europe from which
emissions are only sporadically detected by the existing AGAGE network. We assessed the
added value of a station in FKL, by excluding it from the inversion and estimating Eastern
785   Mediterranean emission only from the existing AGAGE network (S-NFKL). Furthermore, we
excluded all stations but FKL from the inversion to test if the existing AGAGE sites add value
to our estimate of emissions in the Easter Mediterranean (S-OFKL). The regional emission
estimates using the different station setups are shown in Figure 10. For Greece and Turkey,
which were best covered by our observations in FKL, a clear influence of the measurements at
790   FKL on the "top-down" emission estimates can be seen. For HFC-125 and HFC-134a, used as
exemplary compounds for this analysis, the inversion excluding FKL was mainly driven by the
a priori values, whereas including FKL strongly reduced the emissions and the analytic uncer-
tainty (Figure 11). A similar effect is seen for the Middle East and Egypt, although the number
of times during which our site was sensitive to these areas was limited. These results clearly
795   show that regional emission estimates using only AGAGE stations for areas as far as the Eastern
Mediterranean are unreliable and an extension of the current network is critical for emission
control in this economically very dynamic area.

For Eastern European countries and the Balkan regions, the influence of measurements at FKL
reduced HFC-134a and HFC-125 emissions and emission uncertainties slightly. However, Cen-
800   tral European measurements have a similar influence on these results. An interesting impact
over larger distances can be observed for Italy and the Iberian Peninsula, where the additional

measurements from FKL have more of a reducing effect on the absolute emissions than on the uncertainties, whereas emissions in Central and Western Europe including the British Isles are largely unaffected by our measurements at FKL. The effect of measurements at FKL on modelled emissions from Italy and the Iberian Peninsula can be explained by the additional constraints provided by FKL for Italy. These decreased the estimated Italian emissions and at the same time slightly increased baseline mixing ratios for JFJ and CMN for periods with influence from the Western Mediterranean. Since simulated source sensitivities are often simultaneously elevated for Italian and Iberian source areas, the increased baseline will translate also to smaller emissions on the Iberian Peninsula even though the observations at FKL were virtually not sensitive to emissions from this region.

The inversion using only observations from FKL (S-NFKL) had virtually no effect on the a posteriori emissions and their uncertainty for Greece, Turkey, the Eastern region and the Middle East as compared with the BASE inversion. For Egypt, the Maghreb countries and the Balkans slightly reduced a posteriori estimates were observed, whereas for Italy, Central and Western Europe the a posteriori estimates differed strongly from the BASE inversion and showed little uncertainty reduction. These results indicate the importance to include all available halocarbon observations in regional estimates even if these are as distant as Monte Cimone is to Finokalia (~1600 km).

4 Conclusion

During a period of six months, from December 2012 to August 2013, we performed continuous halocarbon observations at the atmospheric observation site of Finokalia (Crete, GR) - the first observations of this kind in the Eastern Mediterranean. The combination of these (and other Western European halocarbon) measurements with an atmospheric transport model, and Bayesian inversion techniques, allowed us to estimate regional-scale halocarbon emissions and for the first time provide reliable "top-town" emission estimates for the Eastern Mediterranean, a region of very diverse economic development and home to approximately 250 million people.

Due to the maritime and remote location of Finokalia, pollution from major metropolitan areas (the closest at a distance of 350-700km) tend to be better mixed into the background atmosphere at their arrival than at other continuous observation sites such as Monte Cimone (Italy) or Jungfraujoch (Switzerland). As expected this lead to generally smaller peak amplitudes for HFC-134a, HFC-125 and HFC-143a in Finokalia, compared to these sites. However, periodic peaks of HFC-152a were unexpectedly high, indicating one or several strong HFC-152a emission

sources within the region directly influencing Finokalia. Higher peak mole fractions than at the
835 Western European observation sites were observed for HCFC-22 and HCFC-142b, because of
continued emissions from Article 5 regions such as Turkey, Egypt and the Middle East.

A range of sensitivity inversions showed that our regional-scale results are largely independent
of the uncertainty assigned to the a priori emissions and the design of the data-model-mismatch
covariance matrix. In general, including off-diagonal elements in the uncertainty covariance
840 matrices and, therefore, considering auto-correlation in the data-mismatch and a-priori uncer-
tainty, led to lower a posteriori emission estimates (BASE and S-ML). Larger discrepancies
between these sensitivity inversions were only seen for Central and Western Europe and HFC-
134a emissions.

Our best estimate of a posteriori ("top-down") emissions and their uncertainties was derived as
845 an average over the five sensitivity inversions and considering their spread and individual ana-
lytical uncertainty. For Article 5 countries in the Eastern Mediterranean (Turkey, Middle East,
Egypt) a posteriori HCFC emissions were in the range assumed in our a priori, whereas they
were smaller for the Non-Article 5 country Greece. In terms of HFC emissions in the Eastern
Mediterranean, we estimated much smaller emissions than reported to the UNFCCC for all
850 analysed compounds in Greece, whereas for Turkey our "top-down" estimates were similar to
UNFCCC-reported values for HFC-125 and HFC-143a, but were much and slightly smaller for
HFC-134a and HFC-152a, respectively. For the remaining regions in the Eastern Mediterranean
no clear trend between "top-down" and our a priori estimates could be established, partly owing
to the very insecure a priori estimates. For the Western and Central European areas of our in-
855 version domain, our "top-down" estimates largely agree with other inverse modelling studies,
although our results are within the lower range of previously reported emissions. Especially for
HFC-134a and HFC-125 we obtained "top-down" estimates up to a factor of two smaller than
reported UNFCCC values for the British Isles, France, Benelux and Germany.

In the context of lower-than-reported HFC-152a emissions from Turkey, the inversion algo-
860 rithm was not able to perfectly simulate periodically measured, large HFC-152a pollution
events at Finokalia. This could either be due to temporally varying emission sources, shortcom-
ings in the atmospheric transport model or an unsuitable inversion setup. The latter two options
can be ruled out since the transport simulation and inversion worked sufficiently well for other
compounds. The first possibility was further analysed by using the temporal correlation be-
865 tween our observations and the simulated source sensitivity within individual grid cells during
and around times when pollution events were observed. This allowed for the localisation of a

possible emission region, located in the northwestern part of Turkey between the Agean coast and the city of Istanbul. The suspected temporal variability in the HFC-152a emissions rather points towards emissions from a HFC production plant than from product application and con-

870   sumption.

Our measurements in Finokalia and the inversely estimated emissions show, that an additional observation site strongly increases the geographic extent and the quality of the inversion results, by reducing the a posteriori emission uncertainties in the Eastern Mediterranean in the range of 40-80% as compared to an inversion only using the Central European AGAGE observations.

875   Including observations from Finokalia reduced estimated Greek HFC-134a emissions by a factor of four, while decreasing the uncertainty by the same factor. Additionally, the location of Finokalia allows the detection of Middle Eastern and North African emissions during specific flow conditions, which is especially interesting due to the restrictions on the use of HCFCs for developing countries by the Montreal Protocol, which recently became effective. However,

880   measurements during several years or a fixed monitoring station would be required to investigate trends in halocarbon emissions, for a continued "top-down" validation of South-Eastern European UNFCCC inventories or for the monitoring of the HCFC phase out in Eastern Mediterranean Article 5 countries.

Acknowledgements

885   This research was funded by the Swiss National Science Foundation (project 200021-137638), the Swiss Federal Office for the Environment (FOEN), and the Swiss State Secretariat for Education and Research and Innovation (SERI). Additional funding was obtained from the EC FP7 project InGOS (Integrated Non-CO2 Greenhouse Gas Observing System; grant agreement number 284274) and trans-national access (TNA) from the EC FP7 ACTRIS Research Infra-

890   structure (grant agreement number 262254). We thank the Finokalia station staff for granting access to the site and supporting the setup and operation of our measurements. The International Foundation High Altitude Research Stations Jungfraujoch and Gornergrat (HFSJG) is acknowledged for the opportunity to perform observations at Jungfraujoch. The logistic at the "O. Vittori" station at Monte Cimone is supported by the National Research Council of Italy.

895 # References

Bergamaschi, P., M. Corazza, U. Karstens, M. Athanassiadou, R. L. Thompson, I. Pison, A. J. Manning, P. Bousquet, A. Segers, A. T. Vermeulen, et al. (2015). Top-down estimates of European CH_4 and N_2O emissions based on four different inverse models, *Atmos. Chem. Phys.*, *15* (2), 715-736, doi: 10.5194/acp-15-715-2015.

900 Bonasoni, P., A. Stohl, P. Cristofanelli, F. Calzolari, T. Colombo, and F. Evangelisti (2000). Background ozone variations at Mt. Cimone Station, *Atmos. Environ.*, *34* (29–30), 5183-5189, doi: 10.1016/S1352-2310(00)00268-5.

Braathen, G. O., A. L. Nohende Ajavon, P. A. Newman, J. Pyle, A. R. Ravishankara, J. F. Bornman, N. D. Paul, X. Tang, S. O. Andersen, and L. Kuijpers (2012). *Handbook for the Montreal Protocol on Substances that* 905 *Deplete the Ozone Layer*, United Nations Environment Programme, Ozone Secretariat, Nairobi, Kenya.

Brunner, D., T. Arnold, S. Henne, A. J. Manning, R. L. Thompson, M. Maione, S. O'Doherty, and S. Reimann (2016). Comparison of four inverse modelling systems applied to the estimation of HFC-125, HFC-134a and SF_6 emissions over Europe, *in preparation*.

Brunner, D., S. Henne, C. A. Keller, S. Reimann, M. K. Vollmer, S. O'Doherty, and M. Maione (2012a). An 910 extended Kalman-filter for regional scale inverse emission estimation, *Atmos. Chem. Phys.*, *12* (7), 3455-3478, doi: 10.5194/acp-12-3455-2012.

Brunner, D., S. Henne, C. A. Keller, M. K. Vollmer, S. Reimann, and B. Buchmann (2012b). Estimating European Halocarbon Emissions Using Lagrangian Backward Transport Modeling and in Situ Measurements at the Jungfraujoch High-Alpine Site, in *Lagrangian Modeling of the Atmosphere*, edited 915 by J. Lin, D. Brunner, C. Gerbig, A. Stohl, A. Luhar and P. Webley, pp. 207-222, American Geophysical Union, Washington, D.C.

Carpenter, L. J., and S. Reimann (Lead Authors) J. B. Burkholder, C. Clerbaux, B. D. Hall, R. Hossaini, J. C. Laube and S. A. Yvon-Lewis (2014). Ozone-Depleting Substances (ODSs) and Other Gases of Interest to the Montreal Protocol, Chapter 1 in *Scientific Assessment of Ozone Depletion: 2014*, Global Ozone 920 Research and Monitoring Project - Report No. 55, World Meteorological Organization, Geneva, Switzerland.

Derwent, R. G., P. G. Simmonds, B. R. Greally, S. O'Doherty, A. McCulloch, A. Manning, S. Reimann, D. Folini, and M. K. Vollmer (2007). The phase-in and phase-out of European emissions of HCFC-141b and HCFC-142b under the Montreal Protocol: Evidence from observations at Mace Head, Ireland and 925 Jungfraujoch, Switzerland from 1994 to 2004, *Atmos. Environ.*, *41* (4), 757-767, doi: 10.1016/j.atmosenv.2006.09.009.

Enting, I. G. (2002). *Inverse Problems in Atmospheric Constituent Transport*, Cambridge University Press, Cambridge, United Kingdom.

Farman, J. C., B. G. Gardiner, and J. D. Shanklin (1985). Large losses of total ozone in Antarctica reveal 930 seasonal CLO_x/NO_x interaction, *Nature*, *315* (6016), 207-210, doi: 10.1038/315207a0.

Ganesan, A. L., M. Rigby, A. Zammit-Mangion, A. J. Manning, R. G. Prinn, P. J. Fraser, C. M. Harth, K. R. Kim, P. B. Krummel, S. Li, et al. (2014). Characterization of uncertainties in atmospheric trace gas inversions using hierarchical Bayesian methods, *Atmos. Chem. Phys.*, *14* (8), 3855-3864, doi: 10.5194/acp-14-3855-2014.

935 Gerasopoulos, E., G. Kouvarakis, M. Vrekoussis, M. Kanakidou, and N. Mihalopoulos (2005). Ozone variability in the marine boundary layer of the eastern Mediterranean based on 7-year observations, *J. Geophys. Res. Atmos.*, *110* (D15), D15309, doi: 10.1029/2005JD005991.

Graziosi, F., J. Arduini, F. Furlani, U. Giostra, L. J. M. Kuijpers, S. A. Montzka, B. R. Miller, S. J. O'Doherty, A. Stohl, P. Bonasoni, et al. (2015). European emissions of HCFC-22 based on eleven years of high frequency 940 atmospheric measurements and a Bayesian inversion method, *Atmos. Environ.*, *112*, 196-207, doi: 10.1016/j.atmosenv.2015.04.042.

Henne, S., D. Brunner, D. Folini, S. Solberg, J. Klausen, and B. Buchmann (2010). Assessment of parameters describing representativeness of air quality in-situ measurement sites, *Atmos. Chem. Phys.*, *10* (8), 3561-3581, doi: 10.5194/acp-10-3561-2010.

945 Henne, S., D. Brunner, B. Oney, M. Leuenberger, W. Eugster, I. Bamberger, F. Meinhardt, M. Steinbacher, and L. Emmenegger (2016). Validation of the Swiss methane emission inventory by atmospheric observations and inverse modelling, *Atmos. Chem. Phys.*, *16* (6), 3683-3710, doi: 10.5194/acp-16-3683-2016.

Herrmann, E., E. Weingartner, S. Henne, L. Vuilleumier, N. Bukowiecki, M. Steinbacher, F. Conen, M.
950 Collaud Coen, E. Hammer, Z. Jurányi, et al. (2015). Analysis of long-term aerosol size distribution data from Jungfraujoch with emphasis on free tropospheric conditions, cloud influence, and air mass transport, *J. Geophys. Res. Atmos.*, *120* (18), 9459-9480, doi: 10.1002/2015JD023660.

Hu, L., S. A. Montzka, J. B. Miller, A. E. Andrews, S. J. Lehman, B. R. Miller, K. Thoning, C. Sweeney, H. Chen, D. S. Godwin, et al. (2015). U.S. emissions of HFC-134a derived for 2008–2012 from an extensive flask-
955 air sampling network, *J. Geophys. Res. Atmos.*, *120* (2), 801-825, doi: 10.1002/2014JD022617.

JRC/PBL (2009). Emission Database for Global Atmospheric Research (EDGAR), release version 4.0, Tech. rep. available at: http://edgar.jrf.ec.europa.eu.

Keller, C. A., D. Brunner, S. Henne, M. K. Vollmer, S. O'Doherty, and S. Reimann (2011). Evidence for under-reported western European emissions of the potent greenhouse gas HFC-23, *Geophys. Res. Lett.*,
960 *38* (15), L15808, doi: 10.1029/2011GL047976.

Keller, C. A., M. Hill, M. K. Vollmer, S. Henne, D. Brunner, S. Reimann, S. O'Doherty, J. Arduini, M. Maione, Z. Ferenczi, et al. (2012). European Emissions of Halogenated Greenhouse Gases Inferred from Atmospheric Measurements, *Environ. Sci. Technol.*, *46* (1), 217-225, doi: 10.1021/es202453j.

Kim, J., S. Li, K. R. Kim, A. Stohl, J. Mühle, S. K. Kim, M. K. Park, D. J. Kang, G. Lee, C. M. Harth, et al. (2010).
965 Regional atmospheric emissions determined from measurements at Jeju Island, Korea: Halogenated compounds from China, *Geophys. Res. Lett.*, *37* (12), L12801, doi: 10.1029/2010GL043263.

Kouvarakis, G., K. Tsigaridis, M. Kanakidou, and N. Mihalopoulos (2000). Temporal variations of surface regional background ozone over Crete Island in the southeast Mediterranean, *J. Geophys. Res. Atmos.*, *105* (D4), 4399-4407, doi: 10.1029/1999JD900984.

970 Levin, I., T. Naegler, R. Heinz, D. Osusko, E. Cuevas, A. Engel, J. Ilmberger, R. L. Langenfelds, B. Neininger, C. v. Rohden, et al. (2010). The global SF$_6$ source inferred from long-term high precision atmospheric measurements and its comparison with emission inventories, *Atmos. Chem. Phys.*, *10* (6), 2655-2662, doi: 10.5194/acp-10-2655-2010.

Lunt, M. F., M. Rigby, A. L. Ganesan, A. J. Manning, R. G. Prinn, S. O'Doherty, J. Mühle, C. M. Harth, P. K.
975 Salameh, T. Arnold, et al. (2015). Reconciling reported and unreported HFC emissions with atmospheric observations, *Proc. Natl. Acad. Sci. U.S.A.*, *112* (19), 5927-5931, doi: 10.1073/pnas.1420247112.

Maione, M., U. Giostra, J. Arduini, F. Furlani, F. Graziosi, E. Lo Vullo, and P. Bonasoni (2013). Ten years of continuous observations of stratospheric ozone depleting gases at Monte Cimone (Italy) — Comments on the effectiveness of the Montreal Protocol from a regional perspective, *Sci. Total Environ.*, *445–446*,
980 155-164, doi: 10.1016/j.scitotenv.2012.12.056.

Maione, M., F. Graziosi, J. Arduini, F. Furlani, U. Giostra, D. R. Blake, P. Bonasoni, X. Fang, S. A. Montzka, S. J. O'Doherty, et al. (2014). Estimates of European emissions of methyl chloroform using a Bayesian inversion method, *Atmos. Chem. Phys.*, *14* (18), 9755-9770, doi: 10.5194/acp-14-9755-2014.

Manning, A. J., D. B. Ryall, R. G. Derwent, P. G. Simmonds, and S. O'Doherty (2003). Estimating European
985 emissions of ozone-depleting and greenhouse gases using observations and a modeling back-attribution technique, *J. Geophys. Res. Atmos.*, *108* (D14), 2156-2202, doi: 10.1029/2002JD002312.

McCulloch, A., P. Ashford, and P. M. Midgley (2001). Historic emissions of fluorotrichloromethane (CFC-11) based on a market survey, *Atmos. Environ.*, *35* (26), 4387-4397, doi: 10.1016/s1352-2310(01)00249-7.

990 Mihalopoulos, N., E. Stephanou, M. Kanakidou, S. Pilitsidis, and P. Bousquet (1997). Tropospheric aerosol ionic composition in the Eastern Mediterranean region, *Tellus B*, *49* (3), 314-326, doi: 10.1034/j.1600-0889.49.issue3.7.x.

Miller, B. R., R. F. Weiss, P. K. Salameh, T. Tanhua, B. R. Greally, J. Mühle, and P. G. Simmonds (2008). Medusa: A Sample Preconcentration and GC/MS Detector System for in Situ Measurements of
995 Atmospheric Trace Halocarbons, Hydrocarbons, and Sulfur Compounds, *Anal. Chem.*, *80* (5), 1536-1545, doi: 10.1021/ac702084k.

Molina, M. J., and F. S. Rowland (1974). Stratospheric sink for chlorofluoromethanes: chlorine atomc-atalysed destruction of ozone, *Nature*, *249* (5460), 810-812, doi: 10.1038/249810a0.

Montzka, S. A., M. McFarland, S. O. Andersen, B. R. Miller, D. W. Fahey, B. D. Hall, L. Hu, C. Siso, and J. W.
1000 Elkins (2015). Recent Trends in Global Emissions of Hydrochlorofluorocarbons and Hydrofluorocarbons: Reflecting on the 2007 Adjustments to the Montreal Protocol, *J. Phys. Chem. A*, *119* (19), 4439-4449, doi: 10.1021/jp5097376.

Myhre, G., D. Shindell, F. M. Bréon, W. Collins, J. Fuglestvedt, J. Huang, D. Koch, J. F. Lamarque, D. Lee, B. Mendoza, et al. (2013). Anthropogenic and Natural Radiative Forcing, in *Climate Change 2013: The*
1005 *Physical Science Basis. Contribution of Working Group I to the Fifth Assessment Report of the Intergovernmental Panel on Climate Change*, edited by T. F. Stocker, D. Qin, G. K. Plattner, M. Tignor, S. K. Allen, J. Boschung, A. Nauels, Y. Xia, V. Bex and P. M. Midgley, pp. 659–740, Cambridge University Press, Cambridge, United Kingdom and New York, NY, USA, doi: 10.1017/CBO9781107415324.018.

O'Doherty, S., D. M. Cunnold, A. Manning, B. R. Miller, R. H. J. Wang, P. B. Krummel, P. J. Fraser, P. G.
1010 Simmonds, A. McCulloch, R. F. Weiss, et al. (2004). Rapid growth of hydrofluorocarbon 134a and hydrochlorofluorocarbons 141b, 142b, and 22 from Advanced Global Atmospheric Gases Experiment (AGAGE) observations at Cape Grim, Tasmania, and Mace Head, Ireland, *J. Geophys. Res. Atmos.*, *109* (D6), D06310, doi: 10.1029/2003JD004277.

O'Doherty, S., D. M. Cunnold, B. R. Miller, J. Mühle, A. McCulloch, P. G. Simmonds, A. J. Manning, S.
1015 Reimann, M. K. Vollmer, B. R. Greally, et al. (2009). Global and regional emissions of HFC-125 (CHF_2CF_3) from in situ and air archive atmospheric observations at AGAGE and SOGE observatories, *J. Geophys. Res. Atmos.*, *114* (D23), D23304, doi: 10.1029/2009JD012184.

Prinn, R. G., R. F. Weiss, P. J. Fraser, P. G. Simmonds, D. M. Cunnold, F. N. Alyea, S. O'Doherty, P. Salameh, B. R. Miller, J. Huang, et al. (2000). A history of chemically and radiatively important gases in air deduced
1020 from ALE/GAGE/AGAGE, *J. Geophys. Res. Atmos.*, *105* (D14), 17751-17792, doi: 10.1029/2000JD900141.

Reimann, S., M. K. Vollmer, D. Folini, M. Steinbacher, M. Hill, B. Buchmann, R. Zander, and E. Mahieu (2008). Observations of long-lived anthropogenic halocarbons at the high-Alpine site of Jungfraujoch (Switzerland) for assessment of trends and European sources, *Sci. Total Environ.*, *391* (2), 224-231, doi: 10.1016/j.scitotenv.2007.10.022.

1025 Rigby, M., J. Mühle, B. R. Miller, R. G. Prinn, P. B. Krummel, L. P. Steele, P. J. Fraser, P. K. Salameh, C. M. Harth, R. F. Weiss, et al. (2010). History of atmospheric SF_6 from 1973 to 2008, *Atmos. Chem. Phys.*, *10* (21), 10305-10320, doi: 10.5194/acp-10-10305-2010.

Rigby, M., R. G. Prinn, S. O'Doherty, B. R. Miller, D. Ivy, J. Mühle, C. M. Harth, P. K. Salameh, T. Arnold, R. F. Weiss, et al. (2014). Recent and future trends in synthetic greenhouse gas radiative forcing, *Geophys.*
1030 *Res. Lett.*, *41* (7), 2623–2630, doi: 1002/2013GL059099.

Ruckstuhl, A. F., S. Henne, S. Reimann, M. Steinbacher, B. Buchmann, and C. Hueglin (2012). Robust extraction of baseline signal of atmospheric trace species using local regression, *Atmos. Meas. Tech.*, *5* (11), 2613-2624, doi: 10.5194/amt-5-2613-2012.

Saikawa, E., M. Rigby, R. G. Prinn, S. A. Montzka, B. R. Miller, L. J. M. Kuijpers, P. J. B. Fraser, M. K. Vollmer,
1035 T. Saito, Y. Yokouchi, et al. (2012). Global and regional emission estimates for HCFC-22, *Atmos. Chem. Phys.*, *12* (21), 10033-10050, doi: 10.5194/acp-12-10033-2012.

Say, D., A. J. Manning, S. O'Doherty, M. Rigby, D. Young, and A. Grant (2016). Re-Evaluation of the UK's HFC-134a Emissions Inventory Based on Atmospheric Observations, *Environ. Sci. Technol.*, *50* (20), 11129-11136, doi: 10.1021/acs.est.6b03630.

1040   Schoenenberger, F., M. K. Vollmer, M. Rigby, M. Hill, P. J. Fraser, P. B. Krummel, R. L. Langenfelds, T. S. Rhee, T. Peter, and S. Reimann (2015). First observations, trends, and emissions of HCFC-31 (CH$_2$ClF) in the global atmosphere, *Geophys. Res. Lett.*, *42* (18), 7817-7824, doi: 10.1002/2015GL064709.

Seibert, P., and A. Frank (2004). Source-receptor matrix calculation with a Lagrangian particle dispersion model in backward mode, *Atmos. Chem. Phys.*, *4*, 51-63, doi: 10.5194/acp-4-51-2004.

1045   Simmonds, P. G., S. O'Doherty, G. Nickless, G. A. Sturrock, R. Swaby, P. Knight, J. Ricketts, G. Woffendin, and R. Smith (1995). Automated Gas Chromatograph/Mass Spectrometer for Routine Atmospheric Field Measurements of the CFC Replacement Compounds, the Hydrofluorocarbons and Hydrochlorofluorocarbons, *Anal. Chem.*, *67* (4), 717-723, doi: 10.1021/ac00100a005.

Simmonds, P. G., M. Rigby, A. J. Manning, M. F. Lunt, S. O'Doherty, A. McCulloch, P. J. Fraser, S. Henne,
1050   M. K. Vollmer, J. Mühle, et al. (2016). Global and regional emissions estimates of 1,1-difluoroethane (HFC-152a, CH$_3$CHF$_2$) from in situ and air archive observations, *Atmos. Chem. Phys.*, *16* (1), 365-382, doi: 10.5194/acp-16-365-2016.

Steinbacher, M., M. K. Vollmer, B. Buchmann, and S. Reimann (2008). An evaluation of the current radiative forcing benefit of the Montreal Protocol at the high-Alpine site Jungfraujoch, *Sci. Total Environ.*,
1055   *391* (2–3), 217-223, doi: 10.1016/j.scitotenv.2007.10.003.

Stohl, A., C. Forster, A. Frank, P. Seibert, and G. Wotawa (2005). Technical note: The Lagrangian particle dispersion model FLEXPART version 6.2, *Atmos. Chem. Phys.*, *5* (9), 2461-2474, doi: 10.5194/acp-5-2461-2005.

Stohl, A., P. Seibert, J. Arduini, S. Eckhardt, P. Fraser, B. R. Greally, C. Lunder, M. Maione, J. Mühle, S.
1060   O'Doherty, et al. (2009). An analytical inversion method for determining regional and global emissions of greenhouse gases: Sensitivity studies and application to halocarbons, *Atmos. Chem. Phys.*, *9* (5), 1597-1620, doi: 10.5194/acp-9-1597-2009.

Taylor, K. E. (2001). Summarizing multiple aspects of model performance in a single diagram, *J. Geophys. Res. Atmos.*, *106* (D7), 7183-7192, doi: 10.1029/2000JD900719.

1065   UN (2016). UN Population Division - World Population Prospects 2015, available from: https://esa.un.org/unpd/wpp/DataQuery/ (Accessed 18 July 2016).

UNFCCC (1997). Kyoto Protocol to the United Nations Framework Convention on Climate Change, available from: http://unfccc.int/kyoto_protocol/items/2830.php (Accessed).

UNFCCC (2016). National Inventory Submissions 2016, available from:
1070   http://unfccc.int/national_reports/annex_i_ghg_inventories/national_inventories_submissions/items/9492.php (Accessed 28 August 2016).

Velders, G. J. M., D. W. Fahey, J. S. Daniel, M. McFarland, and S. O. Andersen (2009). The large contribution of projected HFC emissions to future climate forcing, *Proc. Natl. Acad. Sci. U.S.A.*, *106* (27), 10949-10954, doi: 10.1073/pnas.0902817106.

1075   Velders, G. J. M., A. R. Ravishankara, M. K. Miller, M. J. Molina, J. Alcamo, J. S. Daniel, D. W. Fahey, S. A. Montzka, and S. Reimann (2012). Preserving Montreal Protocol Climate Benefits by Limiting HFCs, *Science*, *335* (6071), 922-923, doi: 10.1126/science.1216414.

Vollmer, M. K., T. S. Rhee, M. Rigby, D. Hofstetter, M. Hill, F. Schoenenberger, and S. Reimann (2015). Modern inhalation anesthetics: Potent greenhouse gases in the global atmosphere, *Geophys. Res. Lett.*,
1080   *42* (5), 1606-1611, doi: 10.1002/2014GL062785.

Vollmer, M. K., L. X. Zhou, B. R. Greally, S. Henne, B. Yao, S. Reimann, F. Stordal, D. M. Cunnold, X. C. Zhang, M. Maione, et al. (2009). Emissions of ozone-depleting halocarbons from China, *Geophys. Res. Lett.*, *36* (15), L15823, doi: 10.1029/2009GL038659.

Xiang, B., P. K. Patra, S. A. Montzka, S. M. Miller, J. W. Elkins, F. L. Moore, E. L. Atlas, B. R. Miller, R. F. Weiss,
1085   R. G. Prinn, et al. (2014). Global emissions of refrigerants HCFC-22 and HFC-134a: Unforeseen seasonal contributions, *Proc. Natl. Acad. Sci. U.S.A.*, *111* (49), 17379-17384, doi: 10.1073/pnas.1417372111.

Zellweger, C., J. Forrer, P. Hofer, S. Nyeki, B. Schwarzenbach, E. Weingartner, M. Ammann, and U. Baltensperger (2003). Partitioning of reactive nitrogen (NO$_y$) and dependence on meteorological

conditions in the lower free troposphere, *Atmos. Chem. Phys.*, *3* (3), 779-796, doi: 10.5194/acp-3-779-
1090   2003.

Table 1: Setup for the base inversion (Base) and the sensitivity inversions (S-XX). Method refers to the uncertainty treatment explained in section 2.7. The sites are abbreviated as follows: Finokalia (FKL), Jungfraujoch (JFJ), Mace Head (MHD) and Monte Cimone (CMN).

Inversion	Method	Sites	Prior emissions uncertainty scaling factor
BASE	Global	FKL, JFJ, MHD, CMN	1
S-ML	Local	FKL, JFJ, MHD, CMN	1
S-MS	Stohl	FKL, JFJ, MHD, CMN	1
S-UH	Global	FKL, JFJ, MHD, CMN	1.5
S-UL	Global	FKL, JFJ, MHD, CMN	0.5
S-NFKL	Global	JFJ, MHD, CMN	1
S-OFKL	Global	FKL	1

1095

Table 2: Inversion performance of the BASE inversion at Finokalia (FKL), Jungfraujoch (JFJ), Mace Head (MHD) and Monte Cimone (CMN). N is the number of observations used for the inversion. RMSE, R^2 and TSS denote the root mean square error, coefficient of determination and the Taylor skill score of the complete signal and R^2_{abg} is the coefficient of determination of the signal above background.

	Site	N	RMSE (ppt)		R^2		R^2_{abg}		TSS	
			apriori	apost	prior	post	prior	post	prior	post
HFC-134a	FKL	1421	4.7	1.7	0.41	0.74	0.20	0.29	0.86	0.95
	JFJ	1946	4.5	3.6	0.33	0.50	0.25	0.34	0.82	0.71
	MHD	2005	3.3	2.9	0.61	0.74	0.61	0.73	0.93	0.75
	CMN	1801	5.8	5.1	0.39	0.54	0.25	0.28	0.62	0.74
HFC-125	FKL	1147	1.4	0.8	0.31	0.59	0.12	0.16	0.81	0.88
	JFJ	1938	1.2	1.2	0.45	0.54	0.34	0.40	0.79	0.74
	MHD	1975	1.0	0.8	0.63	0.74	0.62	0.71	0.88	0.89
	CMN	1840	1.8	1.6	0.42	0.53	0.29	0.32	0.62	0.76
HFC-152a	FKL	1428	4.0	1.2	0.00	0.43	0.00	0.11	0.39	0.62
	JFJ	1960	1.4	1.3	0.36	0.49	0.21	0.31	0.59	0.65
	MHD	2011	0.7	0.5	0.54	0.72	0.26	0.38	0.89	0.90
	CMN	1864	1.5	1.3	0.33	0.55	0.19	0.29	0.54	0.74
HFC-143a	FKL	1252	2.3	1.6	0.06	0.53	0.01	0.03	0.26	0.67
	JFJ	1973	1.2	1.1	0.43	0.48	0.36	0.38	0.83	0.70
	MHD	2052	1.1	0.9	0.63	0.72	0.65	0.71	0.79	0.85
	CMN	1814	1.5	1.4	0.41	0.48	0.31	0.31	0.74	0.72
HCFC-22	FKL	1426	3.7	2.7	0.15	0.42	0.05	0.15	0.52	0.62
	JFJ	1953	2.8	2.1	0.31	0.50	0.14	0.23	0.77	0.73
	MHD	1994	1.8	1.3	0.41	0.65	0.26	0.36	0.84	0.89
	CMN	1728	3.0	2.3	0.35	0.50	0.15	0.19	0.76	0.76
HCFC-142b	FKL	1065	0.6	0.5	0.52	0.64	0.00	0.02	0.79	0.87
	JFJ	1960	0.4	0.3	0.24	0.39	0.12	0.15	0.36	0.62
	MHD	2042	0.2	0.1	0.42	0.66	0.36	0.52	0.64	0.84
	CMN	1802	0.4	0.3	0.48	0.56	0.21	0.19	0.57	0.82

1100

Table 3: Regional emissions as estimated in the a priori inventory and by the atmospheric inversion. All values are given in in Mg yr⁻¹. A posteriori estimates are shown as the mean values, derived from the BASE inversion and the sensitivity inversions S-ML, S-MS, S-UH and S-UL. The uncertainty range gives the maximum range provided by the respective mean values of all inversions plus the mean of the analytic uncertainty ($p < 0.05$) estimated by each individual inversion. Smaller and distant countries were aggregated to larger regions: Turkey (Turkey, Cyprus), Balkans (Serbia, Montenegro, Kosovo, Albania, Bosnia and Herzegovina, Croatia, Slovenia, Macedonia), Eastern (Ukraine, Romania, Moldova, Bulgaria), Middle East (Jordan, Lebanon, Syria, Palestine, Israel), Maghreb (Morocco, Algeria, Tunisia, Libya), Central E (Poland, Slovakia, Czech-Republic, Hungary), Central W (Switzerland, Liechtenstein, Germany, Austria, Denmark), Western (France, Luxembourg, Netherlands, Belgium), Iberian Peninsula (Spain, Portugal), British Isles (Ireland, United Kingdom).

	HFC-134a (CH_2FCF_3)		HFC-125 (C_2HF_5)		HFC-152a ($C_2H_4F_2$)	
	Prior	Post	Prior	Post	Prior	Post
Greece	1.32±0.26	0.42 (0.31-0.63)	0.6 ±0.12	0.25 (0.19-0.31)	1.22±0.49	0.27 (0.21-0.37)
Turkey	2.85±0.58	1.45 (1.00-1.90)	0.12±0.03	0.11 (0.07-0.15)	1.11±0.78	0.62 (0.38-1.05)
Balkans	0.65±0.52	0.70 (0.37-1.03)	0.12±0.1	0.18 (0.08-0.29)	0.15±0.15	0.17 (0.10-0.35)
Eastern	1.15±0.46	0.88 (0.43-1.32)	0.34±0.14	0.32 (0.14-0.49)	0.41±0.29	0.21 (0.05-0.36)
Middle East	0.65±0.64	0.21 (0.00-0.61)	0.14±0.14	0.16 (0.00-0.37)	0.23±0.22	0.19 (0.02-0.35)
Egypt	1.14±1.14	0.94 (0.44-1.43)	0.28±0.28	0.21 (0.01-0.41)	0.46±0.46	0.09 (0.00-0.27)
Maghreb	1.18±1.17	0.89 (0.16-1.62)	0.3 ±0.3	0.39 (0.10-0.68)	0.47±0.47	0.18 (0.05-0.31)
Central E	2.64±0.53	1.57 (1.17-1.98)	1.1 ±0.22	0.76 (0.58-0.94)	0.41±0.16	0.23 (0.14-0.32)
Central W	5.67±1.14	2.40 (1.91-3.18)	0.95±0.19	0.70 (0.55-0.90)	0.38±0.2	0.26 (0.18-0.37)
Western	6.08±1.21	3.13 (2.38-3.84)	1.92±0.38	1.41 (1.24-1.58)	0.44±0.17	0.29 (0.23-0.37)
Italy	1.96±0.39	1.87 (1.64-2.09)	1.06±0.21	1.05 (0.94-1.17)	0.32±0.31	0.26 (0.19-0.32)
Iberian Pen.	4.06±0.82	1.86 (1.33-2.58)	2.03±0.41	1.52 (1.26-1.77)	0.32±0.13	0.16 (0.07-0.25)
British Isles	5.24±1.04	2.68 (2.12-3.54)	1.49±0.3	1.10 (0.99-1.20)	0.21±0.08	0.09 (0.06-0.13)
Domain Total	34.58±9.91	18.99 (31.26-25.76)	10.45±2.81	8.15 (6.15-10.26)	6.12±3.92	2.91 (1.48-4.76)
	HFC-143a ($C_2H_3F_3$)		HCFC-22 ($CHClF_2$)		HCFC-142b ($C_2H_3ClF_2$)	
	Prior	Post	Prior	Post	Prior	Post
Greece	0.17±0.03	0.13 (0.09-0.17)	0.2 ±0.08	0.14 (0.06-0.22)	0.02±0.01	0.015 (0.005-0.024)
Turkey	0.05±0.01	0.05 (0.03-0.06)	1.38±1.39	0.85 (0.18-1.52)	0.11±0.08	0.143 (0.049-0.238)
Balkans	0.08±0.07	0.12 (0.04-0.19)	0.45±0.18	0.30 (0.12-0.48)	0.04±0.01	0.042 (0.023-0.061)
Eastern	0.09±0.04	0.09 (0.04-0.15)	1.51±0.62	0.64 (0.12-1.17)	0.12±0.05	0.075 (0.013-0.136)
Middle East	0.1 ±0.1	0.13 (0.00-0.27)	0.78±0.76	1.00 (0.42-1.82)	0.06±0.04	0.059 (0.000-0.128)
Egypt	0.2 ±0.2	0.27 (0.09-0.44)	1.55±1.55	2.08 (1.41-2.79)	0.13±0.09	0.062 (0.000-0.152)
Maghreb	0.21±0.21	0.45 (0.24-0.67)	1.57±1.57	0.56 (0.12-1.00)	0.13±0.09	0.054 (0.003-0.105)
Central (E)	0.92±0.18	0.60 (0.47-0.74)	1.18±0.47	0.36 (0.07-0.65)	0.1 ±0.04	0.052 (0.017-0.088)
Central (W)	0.65±0.13	0.53 (0.42-0.68)	1.87±0.75	0.62 (0.33-0.98)	0.15±0.06	0.128 (0.094-0.167)
Western	1.49±0.3	1.23 (1.11-1.35)	1.67±0.67	0.76 (0.52-1.00)	0.14±0.05	0.187 (0.159-0.215)
Italy	0.92±0.18	0.74 (0.65-0.83)	1.08±0.43	0.70 (0.52-0.88)	0.09±0.04	0.095 (0.071-0.119)
Iberian Pen.	1.01±0.2	0.99 (0.83-1.16)	1.03±0.41	0.39 (0.10-0.68)	0.08±0.03	0.051 (0.015-0.086)
British Isles	0.77±0.15	0.72 (0.65-0.79)	1.24±0.5	0.67 (0.52-0.81)	0.1 ±0.04	0.071 (0.055-0.087)
Domain Total	6.65±1.8	6.04 (4.64-7.50)	15.51±9.38	9.06 (4.49-13.98)	1.25±0.63	1.034 (0.513-1.606)
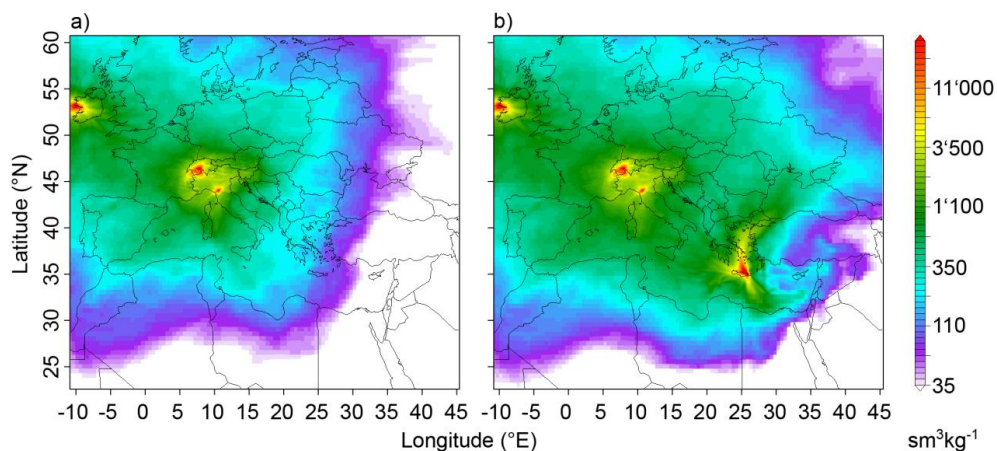
Figure 1: Average FLEXPART derived source sensitivities for the inversions period and domain for a) the measurements at the AGAGE stations Mace Head (MHD), Jungfraujoch (JFJ) and Monte Cimone (CMN) and b) the additional measurements at Finokalia (FKL).

1115
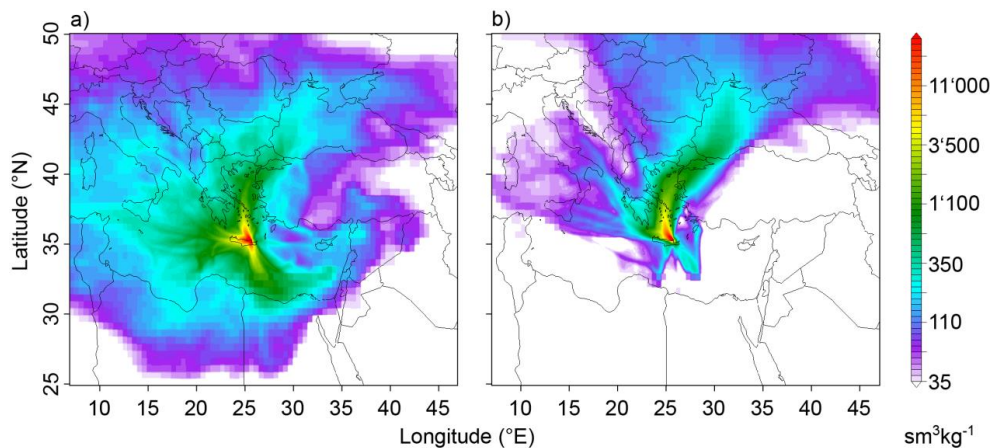
Figure 2: Average FLEXPART derived source sensitivities for Finokalia and two characteristic flow regimes during the measurement campaign: a) shows the variable flow during winter and spring and b) northeasterly flow during the summer months.

1120
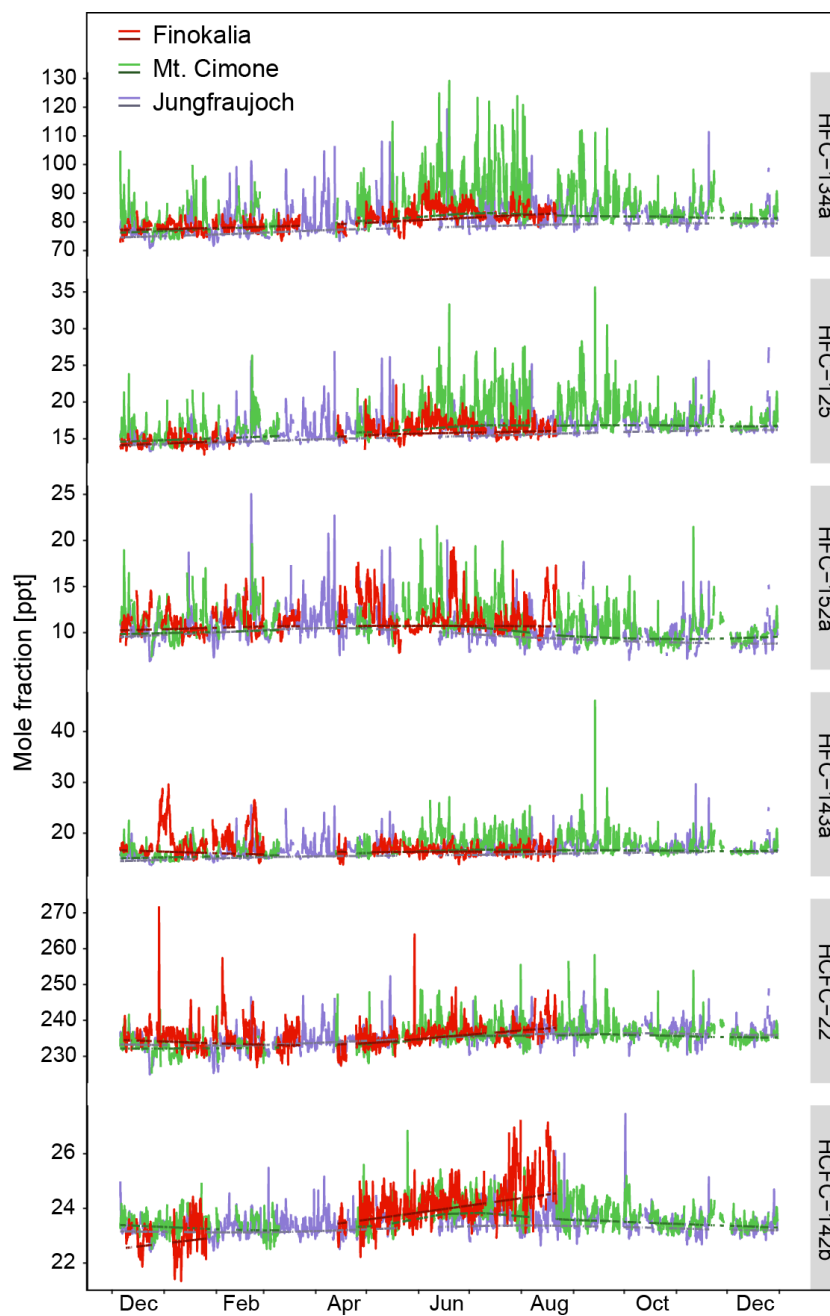
Figure 3: Halocarbon observations in 2013, during the time of the measurement campaign in Finokalia (red) and simultaneous measurements at Jungfraujoch (purple) and Monte Cimone (green). The corresponding background estimated with REBS is shown in the darker shade of the respective color.
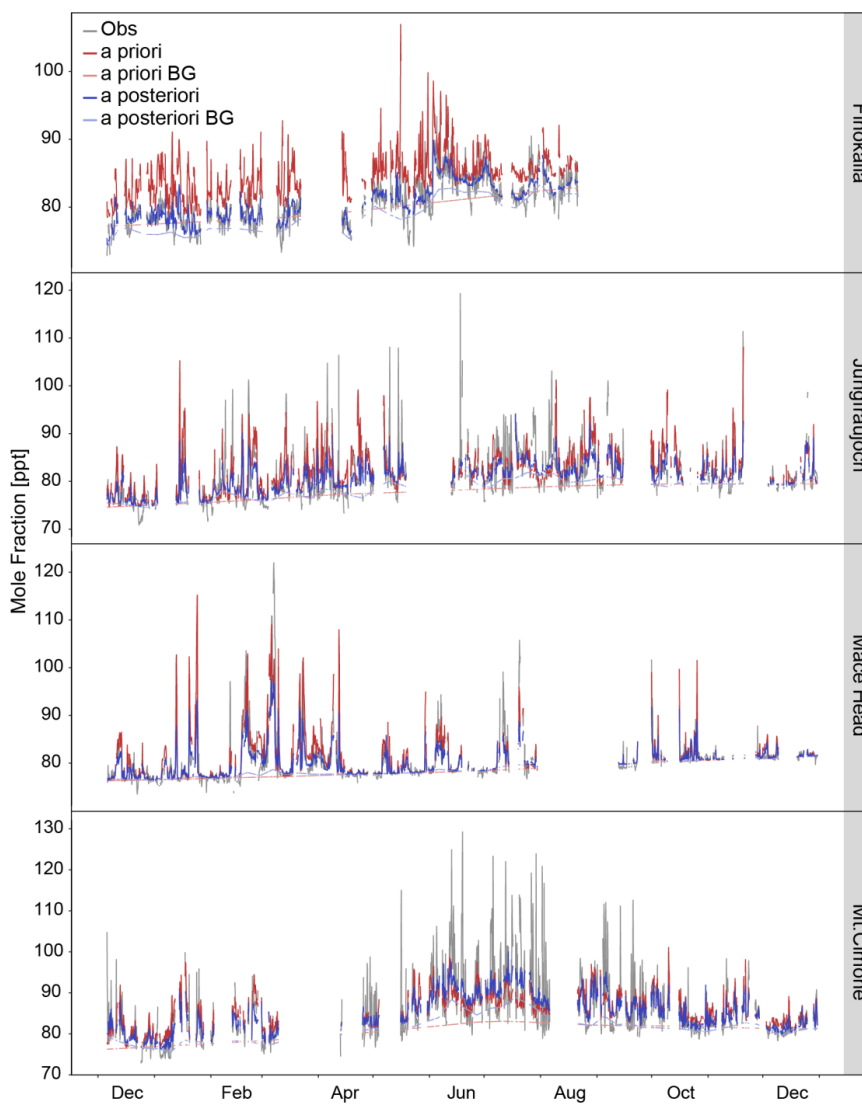
1125

Figure 4: HFC-134a time series of the base inversion for 2013, showing the observed mole fractions at the respective sites (grey) and the simulated values (a priori: red; a posteriori: blue) and their baseline conditions (a priori: light red; a posteriori: light blue).

1130
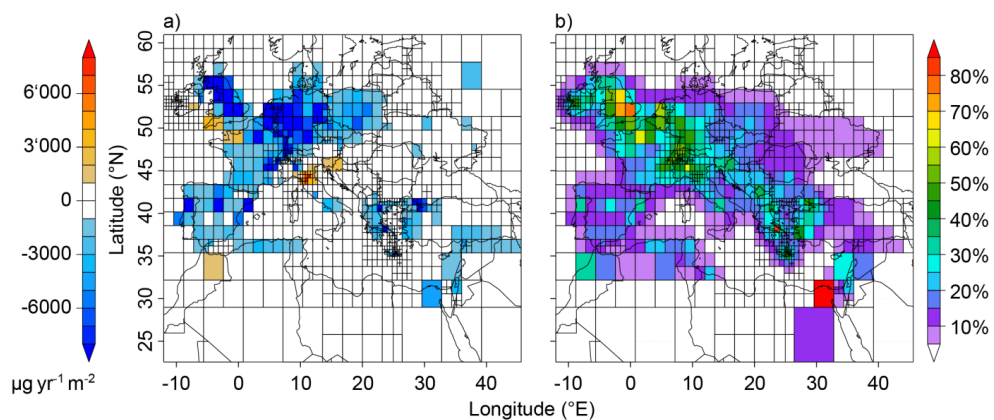
Figure 5: (a) Emissions difference (posterior – prior) of the BASE inversion of HFC-134a. (b) Relative reduction of the a posteriori uncertainty compared to the a priori uncertainties of HFC-134a.
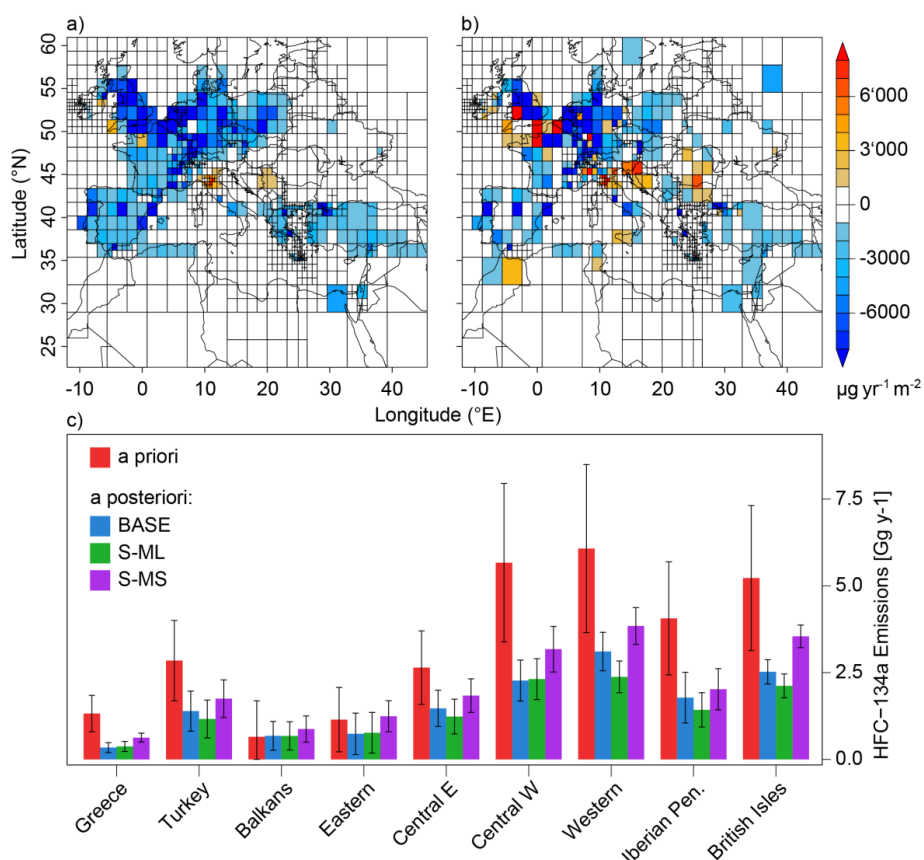
Figure 6: Difference of the a posteriori and a priori emissions for **(a)** the S-ML and **(b)** the S-MS inversions of HFC-134a. **(c)** regional emission estimates: a priori emissions (red) and a posteriori emissions (BASE = green, S-ML = blue, S-MS = purple). The uncertainties given are two standard deviations of the analytic uncertainty assigned to the a priori emissions and derived by the inversion as a posteriori uncertainties.
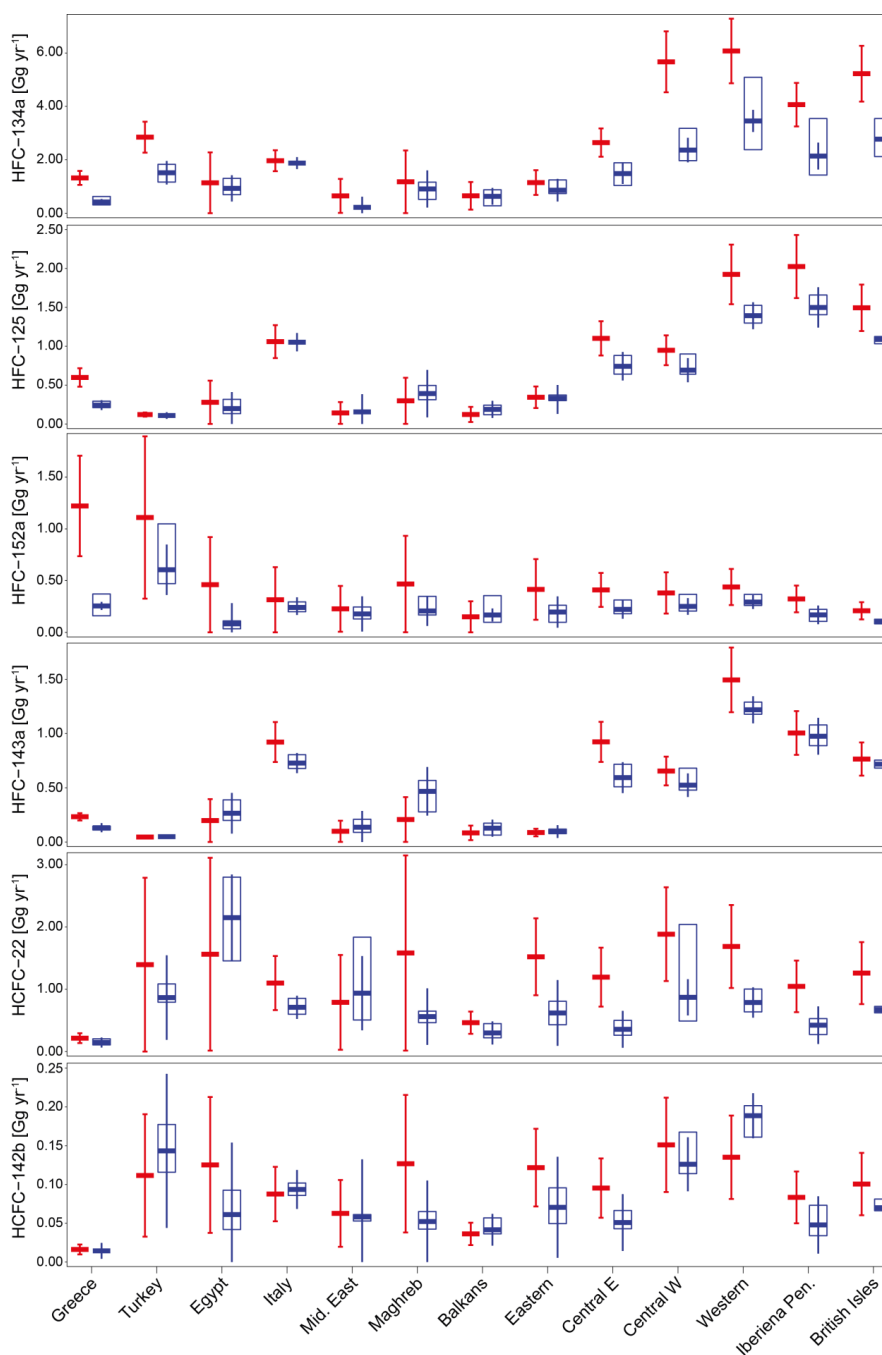
Figure 7: Annual emissions of 2013 for the aggregated regions. A priori emissions are shown in red, with uncertainty giving the 95% confidence range. For the a posteriori estimates boxes show the range of all sensitivity inversions, whereas the thick horizontal line gives the mean of all sensitivity inversions. In addition, the blue error bars give the analytic uncertainty (95% confidence level) averaged over all uncertainty inversions.

1145
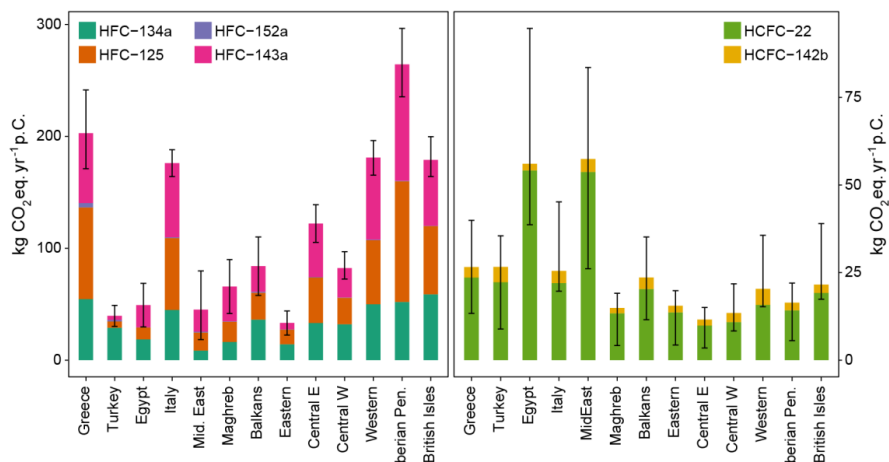
Figure 8: Annual per capita (p.C.) emissions in CO$_2$ equivalents, derived from the base inversion and all sensitivity inversions (best estimate). The results have been computed using the 100-yr GWP (GWP$_{100}$) values of [*Carpenter and Reimann*, 2014]. The bars show the average mean of all inversions, whereas the error bars show our uncertainty estimate including analytical and structural uncertainty.

1150
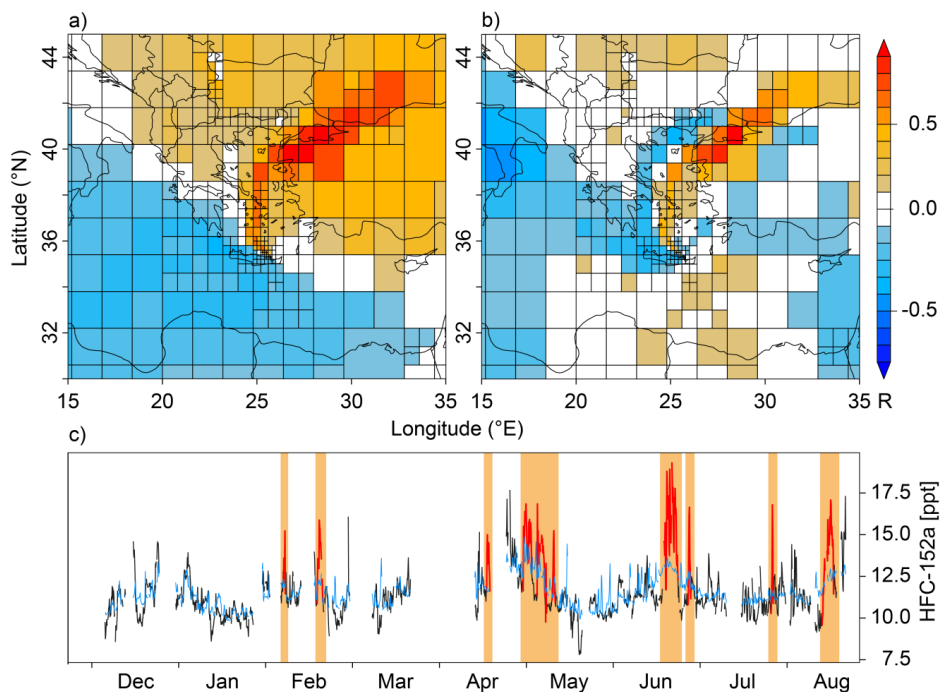
Figure 9: Spatial distribution of the Pearson Correlation Coefficient (R) for (a) the entire time series of HFC-152a observations at Finokalia and the per-cell source sensitivity and for (b) the period of the pollution peaks, which are highlighted in red in (c) the observed (black) and simulated a posteriori (BASE inversion) (blue) mole fractions of HFC-152a.

1155
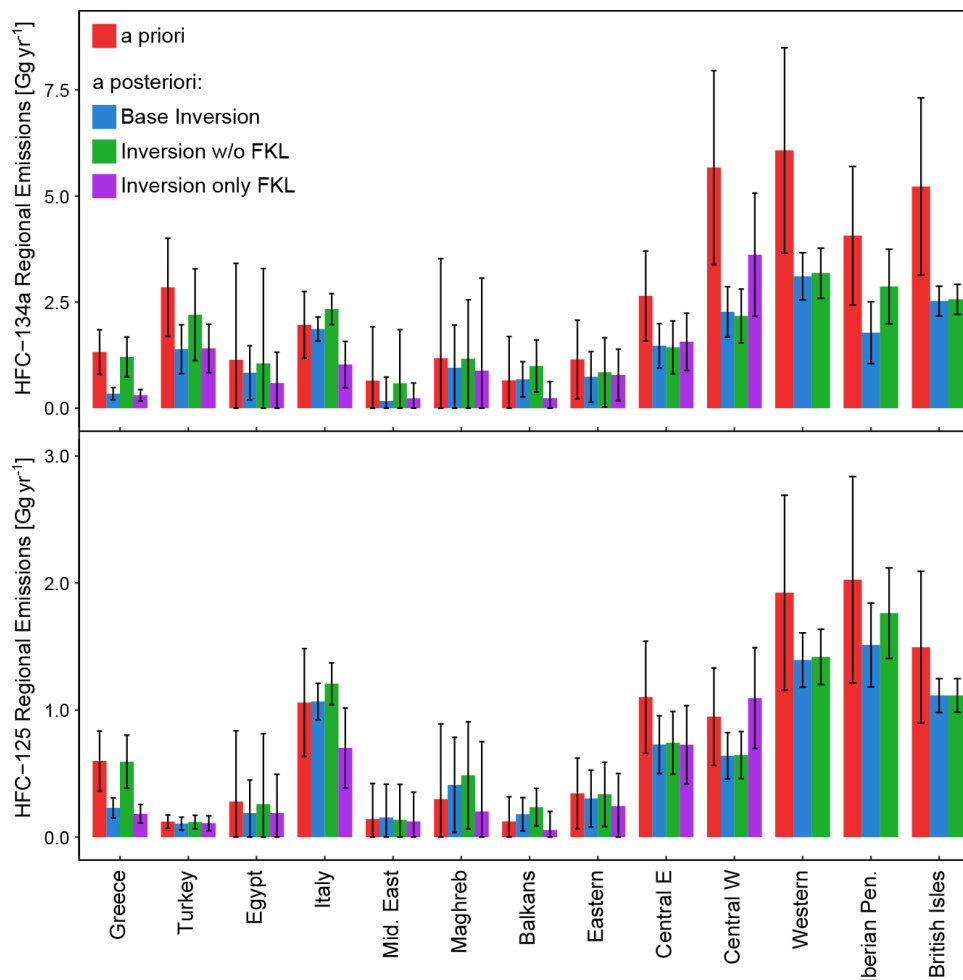
Figure 10: Regional annual emission estimates of 2013. The apriori of our base inversion is shown in red. A posteriori results are shown for the BASE inversion (blue), the inversion excluding Finokalia (S-NFKL, green) and the inversion using only observations from Finokalia (S-OFKL, purple). Error bars represent the 95% confidence levels. Note that for the inversion based on Finokalia observations alone (S-OFKL) the inversion domain was cropped in the West and no a posteriori emission for the western part of the domain were estimated.
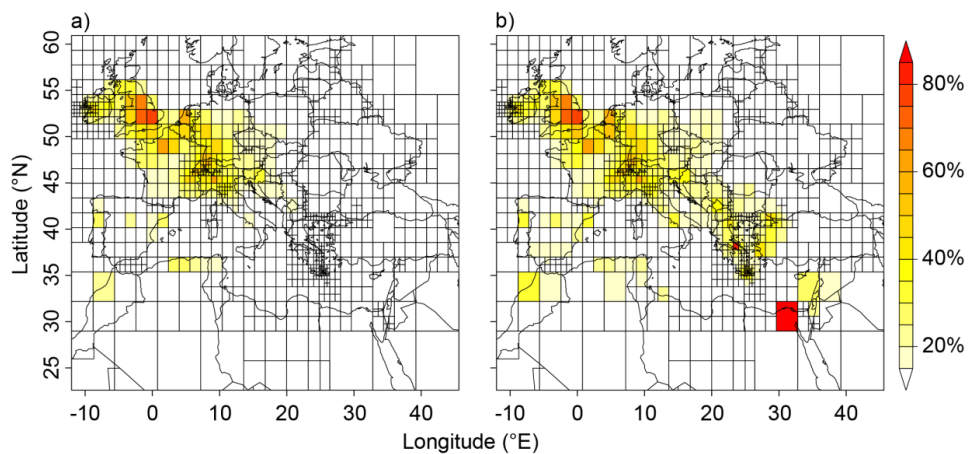
Figure 11: HFC-134a uncertainty reduction (%) achieved by (a) the inversion excluding observations from Finokalia (S-NFKL) and (b) the BASE inversion using observations from all four sites including Finokalia.